CDDpress

www.nature.com/cdd

ARTICLE OPEN

Check for updates

Cell death–induced release of the pro-aging protein acyl CoA binding protein (ACBP) into the circulation

Yan Rong[1,2], Flavia Lambertucci[1], Yaning Yang[1], Vincent Carbonnier[1], Hui Chen[1], Yanbing Dong[1,2], Silvia Mingoia[1], Sijing Li[1], Omar Motiño[1,3], Léa Montégut[1], Adrien Joseph[4,5], Lucille Ferret[1], Ester Gloria Saavedra Díaz[1,6], Stephane Isnard[7,8], Jean-Pierre Routy[7,8,9], Mojgan Djavaheri-Mergny[1], Maria Castedo[1], Alexander Fuerlinger[10,11], Mahmoud Abdellatif[1,10,11], Maria Chiara Maiuri[1,12], Isabelle Martins[1]✉ and Guido Kroemer[1,13,14]✉

Acyl-CoA–binding protein (ACBP, encoded by diazepam binding inhibitor, DBI) is an abundant intracellular regulator of lipid metabolism that also circulates systemically, yet the mechanisms governing its release and its relationship to organ injury remain unresolved. Herein, we combine human multi-omics, mechanistic mouse models and controlled cell death assays to identify cell death–driven liberation of intracellular ACBP/DBI as a unifying mechanism underlying its elevation in disease. In a cohort of 1198 hospitalized adults, among whom 75% were acutely infected by SARS-CoV-2, plasma ACBP/DBI tightly correlated with inflammatory markers and biochemical signatures of cardiac, hepatic, renal, metabolic and hematologic dysfunction. SomaScan proteomics further revealed that ACBP/DBI co-varies with organ-enriched proteins, particularly those originating from skeletal muscle and pancreas, implicating tissue injury as a major determinant of its circulating abundance. Multiple forms of acute organ damage in mice, including hepatic or renal ischemia-reperfusion, bile duct ligation, pancreatitis and rhabdomyolysis, triggered rapid and robust increases in plasma ACBP/DBI. Using defined in vitro paradigms, we demonstrate that apoptosis, ferroptosis and necroptosis each cause loss of intracellular ACBP/DBI and its release upon plasma membrane permeabilization, independent of the upstream lethal pathway. These mechanistic insights translated in vivo: hepatocyte apoptosis, ferroptosis and necroptosis each elevated circulating ACBP/DBI in a manner attenuated by pathway-specific inhibitors. Finally, meta-analysis of >100,000 individuals across diverse populations revealed that elevated plasma ACBP/DBI consistently associates with systemic and organ-specific disease and predicts future morbidity. Together, our findings identify cell death–driven ACBP/DBI release as a conserved mechanism linking organ injury to increased plasma ACBP/DBI, positioning this molecule as an integrative biomarker of tissue damage across species, organs, and cell death modalities.

Cell Death & Differentiation; https://doi.org/10.1038/s41418-026-01775-w

INTRODUCTION

Acyl-CoA–binding protein (ACBP), encoded by the diazepam binding inhibitor gene (*DBI*), is a small (~10 kDa), evolutionarily conserved protein that binds medium- and long-chain acyl-CoA esters with high affinity, thereby regulating intracellular lipid metabolism, energy homeostasis and membrane biogenesis [1, 2]. ACBP/DBI is expressed in all major organs in multiple cell types including parenchymatous and myeloid cells [3], usually as isoform 1, with the sole exception of testicles that also express isoform 2 [4]. Beyond its canonical intracellular functions, ACBP/DBI is secreted in response to metabolic stress, acting as an extracellular signal that modulates systemic energy balance, autophagy and appetite regulation [5–7]. In multiple species, from fungi to mammals, extracellular ACBP/DBI functions as a stress-responsive "tissue hormone," highlighting the evolutionary conservation of its role in coordinating cell-autonomous and systemic homeostasis [8–10]. In both fungi and animals, ACBP/DBI is a leaderless protein that cannot be secreted by canonical protein secretion, but rather employs a non-canonical, autophagy-dependent pathway to reach the extracellular space [8, 11, 12].

Both in yeast and in nematodes, knockout of ACBP/DBI orthologues entails an extension of lifespan [13–16]. In humans,

[1]Centre de Recherche des Cordeliers, Equipe labellisée par la Ligue contre le cancer, Inserm U1138, Université Paris Cité, Sorbonne Université, Paris, France. [2]Faculté de Médecine, Université Paris-Saclay, Le Kremlin Bicêtre, Paris, France. [3]Unidad de Excelencia, Instituto de Biología y Genética Molecular (IBGM), Universidad de Valladolid - CSIC, Valladolid, Spain. [4]Intensive Care Unit, University Hospital Ambroise Pare, GHU Paris-Saclay, AP-HP, Boulogne-Billancourt, France. [5]Inserm U1173, Laboratory of Infection and Inflammation, University Versailles Saint Quentin - University Paris Saclay, Guyancourt, France. [6]Departamento de Bioquímica y Biología Molecular, Fisiología, Genética e Inmunología, Instituto Universitario de Investigaciones Biomédicas y Sanitarias (IUIBS), Universidad de Las Palmas de Gran Canaria, Las Palmas de Gran Canaria, Spain. [7]Infection and Immunity in Global Health Program, Research Institute of the McGill University Health Centre, Montreal, QC, Canada. [8]Chronic Viral Illness Service, McGill University Health Centre, Montreal, QC, Canada. [9]Division of Hematology, McGill University Health Centre, Montreal, QC, Canada. [10]Department of Cardiology, Medical University of Graz, Graz, Austria. [11]BioTechMed, Graz, Austria. [12]Department of Molecular Medicine and Medical Biotechnologies, University of Napoli Federico II, Naples, Italy. [13]Université Paris-Saclay, INSERM US23/CNRS UAR 3655, Metabolomics and Cell Biology Platforms, UMS AMMICa, Institut Gustave Roussy, Villejuif, France. [14]Institut du Cancer Paris CARPEM, Department of Biology, Hôpital Européen Georges Pompidou, AP-HP, Paris, France. ✉email: isabelle.martins@inserm.fr; kroemer@orange.fr

Received: 29 January 2026 Revised: 23 April 2026 Accepted: 20 May 2026
Published online: 03 June 2026

circulating ACBP/DBI has been implicated in aging, metabolic disorders and cardiovascular risk. Plasma levels increase with age, body mass index (BMI) and renal dysfunction and elevated ACBP/DBI predicts future cardiometabolic events and development of cancer independent of traditional risk factors [8, 16–20]. In centenarian and frailty studies, high ACBP/DBI correlates with renal impairment, low-grade inflammation and markers of biological aging [7, 18, 21]. Mechanistically, preclinical studies indicate that neutralization of extracellular ACBP/DBI in mice mitigates obesity, hyperglycemia and age-associated tissue dysfunction, suggesting that ACBP/DBI is not only a biomarker but may also exert a causal influence on metabolic and inflammatory phenotypes [8, 9, 22–25]. Indeed, it appears that ACBP/DBI acts as an inhibitor of autophagy [26, 27], a promoter of inflammatory signaling [22] and an inducer of cellular senescence [7], likely explaining its broad implication in various age-related diseases.

Despite this growing body of evidence, the sources, regulatory mechanisms and pathological contexts underlying elevations in circulating ACBP/DBI remain incompletely understood. It is unclear which organs contribute to plasma ACBP/DBI, whether its release reflects cellular stress or overt cell death and how specific death modalities (apoptosis, ferroptosis or necroptosis) affect its systemic levels. Moreover, while clinical correlations exist, a mechanistic link between tissue injury, cell death and extracellular ACBP/DBI has not been fully established.

We sought to determine whether cell death across multiple organs drives plasma ACBP/DBI elevation and whether this mechanism could explain its correlation with organ dysfunction and disease severity in humans. Using human cohorts, mouse models and in vitro assays, we demonstrate that plasma ACBP/DBI rises in response to apoptosis, ferroptosis and necroptosis across multiple organs. Proteomic analyses identify organ-specific protein signatures correlating with ACBP/DBI, particularly from skeletal muscle and pancreas. Mouse models of liver, kidney, pancreatic and muscle injury recapitulate these findings, while pharmacologic inhibition of specific death pathways suppresses ACBP/DBI release. Meta-analysis of >100,000 individuals confirms associations with age- and organ-specific disease and future disease risk.

MATERIALS AND METHODS

SomaScan-based correlation analyses and tissue enrichment of ACBP/DBI-associated proteins

SomaScan proteomic data together with associated clinical and biological metadata were obtained from an anonymized COVID-19 cohort generated by the Biobanque Québécoise de la COVID-19 (BQC-19) [23, 28]. In that study, participants were recruited upon first contact with the healthcare system (emergency room visit or acute care hospitalization) in Quebec, Canada, between March 2020 and August 2021, following PCR testing for SARS-CoV-2 and included 903 COVID-19-positive adults and 295 hospitalized SARS-CoV-2-negative controls [23, 28].

Plasma ACBP/DBI protein levels were first correlated with numerical clinical variables. Correlation analyses were performed in R using the rcorr function from Hmisc package with default parameters, corresponding to Bravais–Pearson correlation coefficients. Metadata variables were retained if they met all of the following criteria: an absolute correlation coefficient ($|r| \geq 0.3$), a nominal p value ≤ 0.05 and a false discovery rate–adjusted q value ≤ 0.05. Selected variables were visualized using mixed correlation plots generated with the corrplot R package. In these plots, the upper triangular matrix displays signed values of $(1-p$ value), with the sign reflecting the direction of the correlation, whereas the lower triangular matrix displays the corresponding Pearson correlation coefficients (r).

In a second analytical step, plasma ACBP/DBI levels were correlated with all other proteins quantified by the SomaScan platform. Proteins positively correlated with ACBP/DBI were defined as those with a correlation coefficient $r \geq 0.35$, yielding a list of 186 proteins. Based on this number, two additional protein sets were generated: (i) the 186 proteins showing the strongest negative correlations with ACBP/DBI and (ii) a neutral reference set consisting of 372 proteins (2× 186) with correlation coefficients closest to zero. Across all protein sets, SOMAmer reagents annotated as targeting no protein, Fc_MOUSE or deprecated gene labels were excluded. When multiple SOMAmer reagents targeted the same protein, all corresponding entries were excluded to avoid redundancy between protein sets. Following this curation step, ACBP was included in both the anticorrelated and the neutral protein sets. Correlation matrices for each protein set were visualized using corrplots. For the negatively correlated and neutral protein sets, ACBP/DBI was added to the plots to enable direct comparison. Protein lists were subsequently cross-referenced with GTEx tissue expression data extracted from the supplementary dataset published by Zhang and collaborators [29]. For tissue enrichment analyses organs were selected based on GTEx fold-change thresholds of ≥2 or ≥4 relative to other tissues. The GTEx "male" category was excluded due to insufficient annotation accuracy. Tissue enrichment results were expressed as percentages and visualized using bar plots and pie charts [29–31].

Cell culture

Huh7 (human hepatocellular carcinoma) cells were cultured in Dulbecco's modified Eagle's medium (DMEM; Thermo Fisher Scientific, #41966029) supplemented with 10% fetal bovine serum (FBS; Sigma-Aldrich, #F7524), 10 mM HEPES buffer (Thermo Fisher Scientific, #15630–056), 100 U/mL penicillin and 100 µg/mL streptomycin (Thermo Fisher Scientific, #15140-122) and 1 mM sodium pyruvate (Thermo Fisher Scientific, #11360-039). Jurkat (human leukemic T cell lymphoblast) cells were maintained in Roswell Park Memorial Institute medium (RPMI; Thermo Fisher Scientific, #61870044) supplemented with 10% FBS. All cell cultures were maintained at 37 °C in a humidified incubator with 5% CO_2. Mycoplasma contamination was routinely excluded by PCR-based testing.

Induction of apoptosis, ferroptosis and necroptosis in vitro

Huh7 cells were used as a model to study apoptosis and ferroptosis. For apoptosis induction, cells were pre-treated for 1 h with the pan-caspase inhibitor Z-VAD-FMK (Z-VAD; MedChemExpress, #HY-16658B), used at 50 µM for mitomycin C, cisplatin, mitoxantrone and oxaliplatin treatments or at 100 µM for etoposide and thapsigargin treatments. Cells were then exposed for 48 h to mitomycin C (Santa Cruz Biotechnology, #sc-3514A; 50 µM), cisplatin (Sigma-Aldrich, #P4394; 50 µM), mitoxantrone (Sigma-Aldrich, #M6545; 2 µM), oxaliplatin (MedChemExpress, #HY-17371; 100 µM), etoposide (Sigma-Aldrich, #341205; 100 µM) or thapsigargin (Santa Cruz Biotechnology, #sc-24017; 10 µM). For ferroptosis induction, cells were pre-incubated for 1 h with the iron chelator deferoxamine mesylate (DFOM; MedChemExpress, #HY-B0988; 100 µM), followed by treatment for 48 h with imidazole ketone erastin (IKE; Selleckchem, #S8877; 10 µM), RAS-selective lethal 3 (RSL3; Sigma-Aldrich, #SML2234; 0.2 µM) or erastin (MedChemExpress, #HY-15763; 7.5 µM). Necroptosis was induced in Jurkat cells. Cells were pre-incubated for 1 h with a combination of the RIPK1 inhibitor necrostatin-1S (Nec-1S; MedChemExpress, #HY-14622A; 10 µM), the SMAC mimetic xevinapant (AT406; Selleckchem, #S2754; 10 µM) and the pan-caspase inhibitor Q-VD-OPh (MedChemExpress, #HY-12305; 10 µM), followed by treatment with human TNF-α (Thermo Fisher Scientific, #300-01 A; 100 ng/mL) for 24 h.

Imaging flow cytometry analysis

Huh7 cells were collected by harvesting the culture medium followed by trypsin-mediated detachment, after which detached cells were pooled with the corresponding supernatants. Jurkat cells were collected directly from the culture medium. Cells were centrifuged (500 × g, 5 min) and resuspended for subsequent analyses. Cell viability was assessed using the LIVE/DEAD™ Fixable Green Dead Cell Stain Kit (Thermo Fisher Scientific, #L34970) according to the manufacturer's instructions. For intracellular staining, cells were fixed with 4% paraformaldehyde in PBS, permeabilized with 0.1% Triton X-100 in PBS containing BSA and blocked with 2.5% BSA in PBS. Cells were then incubated with an anti-ACBP primary antibody (Santa Cruz Biotechnology, #sc-376853; 1:100 dilution), followed by a PE-Cy7–conjugated secondary antibody (Thermo Fisher Scientific, #25-4015-82; 0.25 µg per test). After washing, cells were analyzed on a BD FACSDISCOVER™ S8 Image Flow Cytometer (BD Biosciences). At least 10,000 events per sample were acquired and data were processed using the BD FACSuite™ Software. Fluorescence intensity was quantified using FlowJo™ software and normalized to the mean fluorescence intensity of the control group. Normalized data are presented as relative fluorescence

intensity. Values below 0.02 were considered non-detectable (ND), corresponding to signals below the limit of reliable quantification, and were therefore excluded from statistical analyses.

Flow cytometry analysis of apoptosis

Apoptosis was assessed using an Annexin V–FITC/propidium iodide (PI) apoptosis detection kit (Thermo Fisher Scientific, #V13245). Following the indicated treatments, Huh7 cells were collected after trypsin-mediated detachment, whereas Jurkat cells were harvested directly from the culture medium. Cell culture supernatants were centrifuged (500 × *g*, 5 min) and aliquots were stored at −80 °C for subsequent ELISA analyses. Cells were pooled, washed once with cold PBS and resuspended in Annexin-binding buffer containing FITC–Annexin V and PI. After incubation for 10 min at room temperature in the dark, samples were diluted with Annexin-binding buffer and analyzed by flow cytometry. Data were acquired on a MACSQuant 10 flow cytometer (Miltenyi Biotec), with at least 10,000 events collected per sample. Data were analyzed using FlowJo™ software.

Ethics and animal models

Mice were housed in a temperature-controlled environment under a 12-h light/dark cycle, with ad libitum access to standard chow (#A04, Safe). All procedures were performed in accordance with the Federation of European Laboratory Animal Science Associations (FELASA) guidelines and approved by the local ethics committee (protocols numbers: #31411-2021050411267667, #34537-2022010210461547, #34538-2022010215486066; #34589-2022010916126141, #46833-2024011116079 08, #58892). Mice were randomly divided into groups.

Acute pancreatitis

Acute pancreatitis was induced in 8-week-old male C57BL/6J mice as previously described [32]. Baseline blood samples were collected one week before treatment. Following a 12-h fast with free access to water, mice received eight intraperitoneal injections of caerulein (MedChemExpress, #HY-A0190; 100 µg/kg body weight (B.W.)) at 1-h intervals, with the first injection designated as time 0. Immediately after the final caerulein injection, mice were administered a single intraperitoneal injection of lipopolysaccharide (LPS; Sigma-Aldrich, #L2630; 10 µg/mouse). Blood samples were collected at 10 h and 12 h after the first caerulein injection.

Rhabdomyolysis

Rhabdomyolysis was induced in 10-week-old male C57BL/6J mice as previously reported [33]. Baseline blood samples were collected one week before treatment. After a 24 h fast with free access to water, mice received intramuscular injections of 50% glycerol (Sigma-Aldrich, #G7893; 5 mL/kg B.W.) in saline administered into both hindlimb muscles. Blood samples were collected at 24 h and 48 h after glycerol administration.

Renal ischemia-reperfusion injury

Renal ischemia–reperfusion injury was induced in 12-week-old male C57BL/6 mice as previously described [34]. Mice were anesthetized with isoflurane and bilateral renal ischemia was induced by transient application of non-traumatic microaneurysm clamps for 30 min. Reperfusion was initiated upon clamp removal and maintained for 6 h. Sham-operated mice underwent identical anesthesia and surgical exposure without clamp application. Blood samples were collected 6 h after reperfusion or at the corresponding time point in sham controls.

Bile duct ligation

Bile duct ligation was performed in 10-week-old male C57BL/6J mice as previously described [35]. Under isoflurane anesthesia, the extrahepatic bile duct was surgically ligated to induce cholestatic liver injury. Sham-operated mice underwent identical surgical procedures without bile duct ligation. Blood samples were collected 14 days after surgery or at the corresponding time point in sham controls.

Liver ischemia-reperfusion injury

Segmental (70%) warm liver ischemia–reperfusion injury was induced in 12-week-old male C57BL/6J mice as previously described [22]. Under isoflurane anesthesia, partial hepatic ischemia was induced by transient occlusion of the portal triad supplying the left and median lobes, while perfusion of the right and caudate lobes was preserved. Ischemia was maintained for 90 min, followed by reperfusion upon clamp removal. Baseline blood samples were collected prior to ischemia and post-reperfusion samples were collected 4 h after reperfusion.

Experimental models of hepatic apoptosis, ferroptosis and necroptosis in mice

To induce hepatocyte apoptosis, female *Atg4b*$^{-/-}$ and *Atg4b*$^{+/+}$ mice [36], as well as 10-week-old male C57BL/6J mice, received intraperitoneal injections of the anti-Fas/CD95 antibody Jo-2 (BD Biosciences, #554254; 0.15 µg/g B.W.). In C57BL/6J mice, the pan-caspase inhibitor Z-VAD (5 mg/kg B.W.), prepared in 10% DMSO in corn oil, was administered intraperitoneally 1 h prior to Jo-2 injection. Blood samples were collected 4 h and 6 h after treatment.

For liver-specific ACBP deletion, tamoxifen-inducible TTR-cre^{+} ACBP$^{fl/fl}$ mice and Cre-negative ACBP$^{fl/fl}$ littermate controls [37] received tamoxifen (Sigma, #T5648; 75 mg/kg B.W.) intraperitoneally once daily for five consecutive days. Experiments were performed two weeks after the final tamoxifen injection. Cre-positive mice were referred to as liver ACBP$^{-/-}$ and Cre-negative mice as Liver ACBP$^{+/+}$ controls. To induce hepatocyte ferroptosis, liver ACBP$^{-/-}$ mice, liver ACBP$^{+/+}$ mice and 12-week-old male C57BL/6J mice were fasted for 16 h prior to intraperitoneal administration of acetaminophen (APAP; Sigma-Aldrich, #A7085; 300 mg/kg B.W.) dissolved in 10% ethanol/90% phosphate-buffered saline. In C57BL/6J mice, the iron chelator deferoxamine mesylate (DFOM; 200 mg/kg B.W.) prepared in PBS was administered intraperitoneally 1 h before APAP. Blood samples were collected 16 h and 24 h after APAP injection.

To induce necroptosis in the liver, 10-week-old male C57BL/6J mice received intraperitoneal injections of mouse TNF-α (Thermo Fisher Scientific, #315-01A; 30 µg/kg B.W.) in combination with D-galactosamine (D-Gal; Sigma-Aldrich, #G0500; 250 mg/kg B.W.). The RIPK1 inhibitor necrostatin-1S (Nec-1S; 6 mg/kg B.W.), prepared in 2.5% DMSO in PBS, was administered intravenously 1 h prior to TNF-α/D-Gal treatment. Blood samples were collected 6 h after injection.

Blood and tissue collection

Blood samples were collected in lithium–heparin capillary tubes (Microvette® CB 300 LH, Sarstedt) and kept on ice prior to centrifugation (4000 × *g*, 10 min). Plasma was separated and stored at −80 °C until further analysis. For molecular analyses, livers were excised immediately after euthanasia and snap-frozen in liquid nitrogen.

Human and mouse ACBP/DBI ELISA

ACBP/DBI concentrations in cell culture supernatants and mouse plasma were quantified by ELISA as previously described [37]. High-binding 96-well plates were coated overnight at 4 °C with human anti-ACBP/DBI capture antibody (MyBioSource, #MBS768488; 1 µg/mL in PBS) or mouse anti-ACBP/DBI capture antibody (Abcam, #ab231910; 1 µg/mL in PBS). Plates were washed and blocked with 1% BSA/0.05% Tween-20 in PBS for 2 h at room temperature. Diluted samples (cell culture supernatants, 1:25; mouse plasma, 1:20) or standards were incubated for 2 h at room temperature, followed by incubation with species-matched detection antibodies (human: Lifespan Biosciences, LS-C299614; mouse: MyBioSource, #MBS2005521; 1 µg/mL) for 1 h. Plates were then incubated with HRP-conjugated avidin (cell culture supernatants, 1:5000; mouse plasma, 1:1000) for 30 min. Signal was developed using 1-Step Ultra TMB substrate (Thermo Fisher Scientific, #34029), stopped with 2 M H_2SO_4 and absorbance was measured at 450 nm using a VICTOR Nivo Multimode Microplate Reader (PerkinElmer).

Plasma hepatic transaminases determination

Alanine aminotransferase (ALT) and Aspartate aminotransferase (AST) activities were measured using colorimetric kits (Randox) according to the manufacturer's instructions [21].

Blood urea nitrogen (BUN) determination

BUN was measured in plasma using the Urea Nitrogen Colorimetric Detection Kit (Thermo Fisher Scientific, #EIABUN) according to the manufacturer's instructions.

Immunoblot

Liver samples were lysed in RIPA buffer (Sigma-Aldrich, #R0278) supplemented with protease (Sigma-Aldrich, #11836170001) and phosphatase inhibitors (Sigma-Aldrich, #04906837001). Lysates were clarified by

centrifugation (13,000 × *g*, 30 min, 4 °C) and protein concentrations were determined using the BCA assay (Thermo Fisher Scientific, #23225). Equal amounts of protein were denatured in loading buffer with reducing agent, resolved by SDS–PAGE and transferred onto polyvinylidene fluoride membranes. Membranes were stained with Ponceau S, imaged to assess total protein loading, then blocked with 5% BSA and incubated with a primary anti-mouse ACBP/DBI antibody (Abcam, #ab231910; 1:1000), followed by HRP-conjugated secondary antibodies. β-actin (Abcam, #49900; 1:5000), GAPDH (Abcam, #9482; 1:5000) or Ponceau S staining was used as a loading control. Signals were detected using the ImageQuant LAS4000 system and band intensities were quantified with ImageJ software.

Senescence-associated secretory phenotype (SASP) score

The SASP protein panel was defined by combining previously published lists from ref. [38] and KEGG hsa04218 cellular senescence pathway (KEGGREST v1.46.0). To ensure proper matching with the SomaScan dataset, gene symbols were retrieved from org.Hs.eg.db (v3.20.0) and mapped to their respective protein symbols using AnnotationDbi (v1.68.0). A total of 46 SASP proteins (HIPK3, CHEK1, CHEK2, MAPK14, EIF4EBP1, AKT2, RRAS2, FOXM1, FOXO3, IGFBP3, IL1A, IL6, CXCL8, SMAD2, SMAD3, MDM2, MRE11, NFATC1, SERPINE1, PPID, MAPK1, MAPK3, MAP2K1, PTEN, RAD1, RAF1, RB1, RBBP4, RRAS, TGFB1, TGFB2, TGFB3, TP53, CCNA1, CCNB2, INHBC, FAS, IL7, CCL2, MMP1, MMP7, MMP9, CCL5, SOST, TNF, VEGFA) were detected out of which a composite senescence score was derived by summing within-protein ranks across the SASP panel. Specifically, participants were ranked for each protein by plasma level (highest = largest rank) and ranks (ties averaged) were then summed and z-scaled to obtain the senescence score. Associations between the senescence score and ACBP levels were calculated using Spearman correlation. Analysis was performed in R version 4.4.1 (R Foundation for Statistical Computing, Vienna, Austria) and GraphPad Prism 10.

Data analysis

Data are presented as mean ± SEM, box-and-whisker plots (median, interquartile range and full range with individual data points) or scatter plots with linear regression where appropriate. Normality was assessed using the Shapiro–Wilk test. For each biological parameter, statistical comparisons were conducted after exclusion of outliers using the ROUT test (Q = 1%, GraphPad Prism 10), resulting in the removal of <1% of data points. Paired comparisons were performed using paired Student's *t* tests, while unpaired comparisons between two groups used Student's *t* tests or Mann–Whitney *U* tests, as appropriate. For normally distributed data, multiple comparisons were analyzed using one-way ANOVA followed by Šidák's post hoc test. For non-normally distributed data, multiple comparisons were analyzed using the Kruskal–Wallis test followed by Dunn's post hoc test. Correlations were assessed using Pearson's or Spearman's methods according to data distribution. Statistical significance was defined as $p < 0.05$. All analyses were performed using GraphPad Prism 10.

Bibliographic analysis of circulating ACBP/DBI-associated parameters

A structured bibliographic analysis was performed to summarize published associations between circulating ACBP/DBI levels (measured by ELISA, O-link or Somascan technologies) and clinical or biological parameters in human cohorts. Only human studies providing analyzable associations with defined parameters were included, if associations with plasma ACBP/DBI levels were significant, as calculated by the authors of each study.

For each eligible study (which are all cited in Fig. 7; Supplementary Table 1), total number of individuals and number of independent cohorts, demographic, biochemical or biophysical parameters, and clinical categories were extracted, usually from supplemental Xcel files. Parameters were grouped into thematic categories encompassing aging, body composition, metabolic traits, inflammatory markers, cardiovascular, renal and hepatic function, infectious, inflammatory, oncological, neurological and psychiatric disorders, morbidity and frailty, as well as future risk outcomes. When applicable, multiple cohorts reported within a single study were counted separately.

Data were summarized graphically using color-coded representations of cumulative sample size and dot-based annotations indicating the number of independent cohorts. This analysis was descriptive and did not involve meta-analytic weighting or additional statistical testing.

RESULTS

Correlation of plasma ACBP/DBI with organ-specific proteins in a cohort of COVID-19 patients

In a cohort composed of 903 SARS-CoV-2–infected adults and 295 non-infected hospitalized controls [23, 39, 40], ACBP/DBI plasma levels increased with the severity of coronavirus disease 2019 (COVID-19). ACBP/DBI levels were higher in patients with comorbidities, including diabetes, obesity, cardiovascular disease, chronic obstructive pulmonary disease and cancer and correlated with inflammatory markers such as the neutrophil to lymphocyte ratio, the hepatocyte product C-reactive protein (CRP) and the more broadly produced interleukin-6 (IL-6) [23]. Beyond these published findings, we observed that ACBP/DBI is associated with the duration of hospitalization, elevated serum creatinine and urea levels (reflecting impaired renal function), hyperglycemia, increased circulating troponin T (indicating cardiac injury), as well as reduced hemoglobin and albumin levels (Supplementary Fig. S1A). ACBP/DBI also correlated with a compendium of proteins annotated as components of the senescence-associated secretory phenotype (SASP) (Supplementary Fig. S1B). We correlated ACBP/DBI concentrations in plasma with those of ~5000 other proteins measured by SomaScan proteomics, to identify 185 proteins that positively correlated with ACBP/DBI with a Spearman correlation coefficient ≥0.35 (Fig. 1A).

We identified 353 proteins showing no correlation (r values between −0.0078680 and 0.0079278) with ACBP/DBI and 174 proteins that strongly ($r \leq -0.1791$) anti-correlate with ACBP/DBI (Supplementary Fig. S3A).

To determine the putative organ of origin of these proteins, we applied a published bioinformatic definition in which an "organ-specific" protein is encoded by an mRNA species expressed at least four-fold higher in one organ compared to all others [41]. Strikingly, two organs, skeletal muscle and pancreas, were strongly enriched among proteins positively correlated with ACBP/DBI (Fig. 1B), whereas proteins lacking correlation or showing anti-correlation did not display such enrichment (Supplementary Figs. S2, S3B; Fig. 1C).

In summary, plasma ACBP/DBI levels increase across multiple pathological conditions and associate with organ-derived protein signatures, prominently those from skeletal muscle and pancreas in the context of COVID-19.

Organ damage causes a surge in plasma ACBP/DBI in mice

Quantitative immunoblotting of hepatic extracts allowed us to estimate that 1 g of liver contains ~62.6 µg of ACBP/DBI (Supplementary Fig. S4A). This value enabled us to extrapolate the ACBP/DBI content of other organs using prior comparative data [3] (Supplementary Fig. S4B). Thus, 1 g of kidney, pancreas or skeletal muscle is predicted to contain 15.6 µg, 6.8 µg or 2.8 µg of ACBP/DBI, respectively. Mouse–human comparisons further indicated that the organ-specific distribution of ACBP/DBI expression is conserved across species (Supplementary Fig. S4C). Given that a ~25 g mouse contains ~5 ml of extracellular water [42, 43] and that the physiological plasma concentration of ACBP/DBI is ~25 ng/ml [22], the total extracellular ACBP/DBI pool amounts to ~125 ng. Hence, the release of ACBP/DBI from only ~2 mg of liver, 8 mg of kidney, 18 mg of pancreas or 44 mg of skeletal muscle would suffice to double its extracellular concentration.

Consistent with this prediction, acute or subacute injury to pancreas, skeletal muscle, kidney or liver caused rapid increases in circulating ACBP/DBI. Caerulein-induced pancreatitis triggered a robust rise in plasma ACBP/DBI (Fig. 2A–C for males; Supplementary Fig. S5A–C for females). Similarly, intramuscular glycerol injection leading to rhabdomyolysis elicited a marked elevation of plasma ACBP/DBI (Fig. 2D–F). Renal ischemia-reperfusion injury also led to significant increases in plasma ACBP/DBI concomitant with a surge in blood urea nitrogen (BUN) as a sign of kidney failure (Fig. 2G–I; Supplementary Fig. S5D). Subacute hepatobiliary injury following bile duct ligation (Fig. 2J–M) and acute hepatic

ischemia–reperfusion also led to significant increases in plasma ACBP/DBI (Fig. 2N–Q), with both ALT and AST strongly correlating with ACBP/DBI (Supplementary Fig. S5E–H).

Taken together, these results demonstrate that chemically or surgically induced organ damage, regardless of tissue type, rapidly increases extracellular ACBP/DBI concentrations.

Cell death is coupled to ACBP/DBI release in vitro

We next investigated which major cell death modalities—apoptosis, ferroptosis or necroptosis—trigger the release of intracellular ACBP/DBI. To this end, we established conditions under which human liver Huh7 cells underwent apoptosis, induced by cisplatin and blocked by the pan-caspase inhibitor

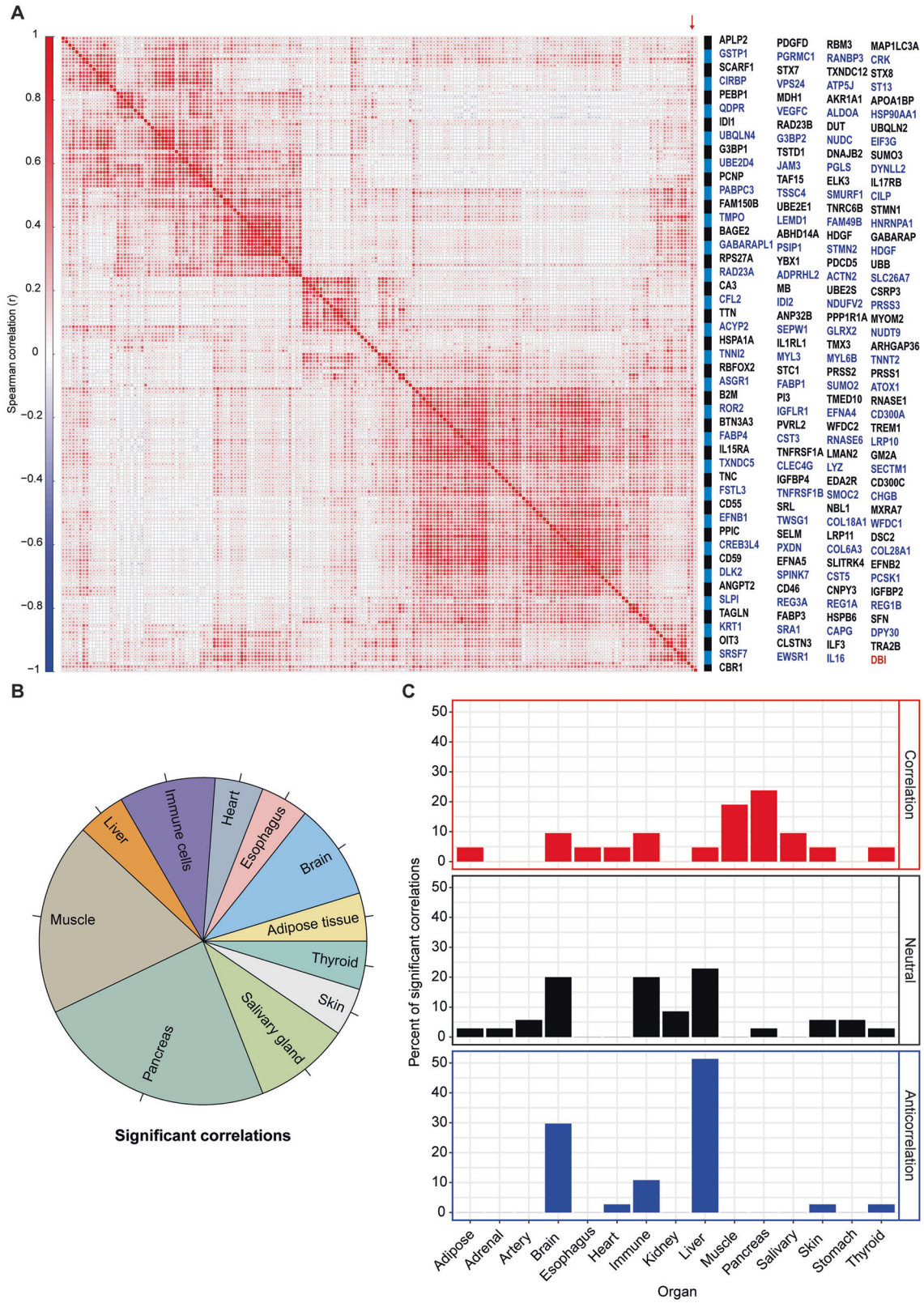

Fig. 1 Correlation of plasma ACBP/DBI with organ-enriched protein signatures in hospitalized COVID-19 patients. A Spearman correlation matrix showing pairwise correlations between plasma ACBP/DBI concentrations and 186 SomaScan-measured plasmatic proteins positively correlated with ACBP/DBI (Spearman $r \geq 0.35$) in a cohort of 903 SARS-CoV-2–infected patients and 295 non-infected hospitalized controls. The red arrow indicates the position of ACBP/DBI within the correlation matrix. Color scale indicates Spearman correlation coefficients (r), ranging from −1 (blue) to +1 (red). **B** Distribution of organ origin among proteins positively correlated with plasma ACBP/DBI. Organ specificity was assigned using a published bioinformatic definition, whereby an organ-enriched protein is encoded by an mRNA expressed at least four-fold higher in one organ compared to all others. Pie chart indicates the relative contribution of each organ to the set of ACBP/DBI-correlated proteins. **C** Comparative analysis of organ enrichment across three protein groups: positively correlated with ACBP/DBI (red; $r \geq 0.35$), non-correlated (black; $-0.0078680 \leq r \leq 0.0079278$) and anti-correlated (blue; $r \leq -0.1791$). Bar plots show the percentage of proteins assigned to each organ within each group.

benzyloxycarbonyl-valyl-alanyl-aspartyl-fluoromethyl ketone (Z-VAD) (Fig. 3A–C) or ferroptosis, induced by imidazole ketone erastin (IKE) and prevented by the iron chelator deferoxamine mesylate (DFOM) (Fig. 3D–F). We also optimized the conditions under which human Jurkat cells underwent necroptosis, induced by the combination of three agents—namely, the caspase inhibitor quinoline-valyl-aspartyl-(O-phenoxy)-methyl ketone (Q-VD-OPh), TNF-α and the SMAC mimetic AT406 (collectively termed QTA)—and suppressed by the RIPK1 inhibitor necrostatin-1S (Nec-1S) (Fig. 3G–I).

Cells were stained with a Live/Dead amine-reactive dye to detect loss of plasma membrane integrity and associated membrane alterations, resulting in green fluorescence in non-viable cells and were subsequently subjected to immunofluorescence detection of intracellular ACBP/DBI using a primary antibody followed by a red-fluorescent secondary. Viable control cells displayed strong intracellular ACBP/DBI staining, whereas apoptotic, ferroptotic or necroptotic cells uniformly lost this signal, as quantified by fluorescence flow cytometry (Fig. 3A, D, G) and confirmed by image cytometry (Fig. 3B, E, H). In all conditions, intracellular ACBP/DBI levels were significantly higher in live cells than in dead cells (Fig. 3C, F, I).

We next measured extracellular ACBP/DBI by ELISA in the supernatant of cells exposed to six apoptosis inducers (mitomycin C, cisplatin, mitoxantrone, oxaliplatin, etoposide or thapsigargin), three ferroptosis inducers (IKE, RSL3 or erastin) or the necroptosis inducing cocktail QTA, with or without their respective inhibitors. Using annexin-V–FITC and propidium iodide (PI) staining to track early apoptosis and late membrane rupture (Fig. 4A), we observed that extracellular ACBP/DBI concentrations increased proportionally as cells transitioned through early cell death toward terminal plasma membrane permeabilization (Fig. 4B). Accordingly, ACBP/DBI release positively correlated with early death, indicated by annexin-V positivity and PI^{low} status (Fig. 4C), late membrane rupture, indicated by PI positivity (Fig. 4D), as well as the sum of all death events (Fig. 4E).

Together, these results show that ACBP/DBI is not selectively released by a particular cell death pathway but is instead liberated whenever plasma membrane integrity is lost, regardless of whether cells undergo apoptosis, ferroptosis or necroptosis.

Apoptosis, ferroptosis and necroptosis cause an increase in plasma ACBP/DBI in mice

We next asked whether the death-modality–dependent release of intracellular ACBP/DBI observed in vitro is recapitulated in vivo. To investigate apoptosis-induced ACBP/DBI release in the context of impaired autophagy, we used *Atg4b*$^{-/-}$ mice, which exhibit partial autophagy deficiency, alongside *Atg4b*$^{+/+}$ littermate controls [36, 44]. In contrast to *Atg4b*$^{+/+}$ mice, *Atg4b*$^{-/-}$ mice failed to elevate plasma ACBP/DBI in response to a 48-h starvation challenge (Fig. 5A–C), confirming their known defect in autophagy-dependent ACBP/DBI secretion [8]. To induce apoptosis in hepatocytes, we injected the anti-Fas/CD95 antibody Jo-2 [45] intraperitoneally into *Atg4b*$^{+/+}$ mice or *Atg4b*$^{-/-}$ mice. Jo-2 administration induced comparable hepatocellular apoptosis in *Atg4b*$^{+/+}$ and *Atg*4b$^{-/-}$ mice, evidenced by a robust increase in serum ALT and AST (Fig. 5D, E). This apoptotic insult caused a parallel rise in plasma ACBP/DBI in both genotypes (Fig. 5F), indicating that Jo-2–induced ACBP/DBI release is autophagy-independent. As expected [46], co-treatment with the pan-caspase inhibitor Z-VAD markedly suppressed the Jo-2–induced rise in transaminases (Fig. 5G–K). This hepatoprotective effect was mirrored by a strong reduction in Jo-2–triggered ACBP/DBI elevation (Fig. 5L, M) and plasma ACBP/DBI levels closely correlated with ALT and AST (Supplementary Fig. S6A–D). Concordantly, Jo-2 decreased hepatic ACBP/DBI protein abundance (Supplementary Fig. S6E, F). These results, obtained in both female (Fig. 5A–F) and male (Fig. 5G–M) mice, demonstrate that selective activation of apoptosis in one organ is sufficient to increase circulating ACBP/DBI.

N-acetyl-para-aminophenol (APAP; acetaminophen/paracetamol) overdose causes acute liver failure (~500 annual U.S. deaths) [47] and induces ferroptosis in hepatocytes [48]. We injected APAP into control mice (liver ACBP$^{+/+}$ mice) and into liver ACBP$^{-/-}$ mice [49], in which hepatocyte-specific excision of the floxed DBI exon 2 abolishes ACBP/DBI expression (Supplementary Fig. S7A, B). Liver-specific ACBP/DBI deletion [37, 49] conferred marked protection against APAP-induced hepatotoxicity, as shown by strongly reduced ALT, AST and plasma ACBP/DBI elevations (Fig. 6A–D). APAP tends to reduce hepatic ACBP/DBI protein levels (Supplementary Fig. 8A, B), further supporting hepatocytes as the primary source of APAP-induced ACBP/DBI release. The ferroptosis inhibitor DFOM [50, 51] efficiently suppressed APAP-triggered release of transaminases and ACBP/DBI (Fig. 6E–K; Supplementary Fig. 8C–F).

To model necroptotic hepatocyte death, we used TNF-α in combination with D-galactosamine (D-Gal) [52]. This combination induced a significant rise in circulating ACBP/DBI, which was partially inhibited by the RIPK1 inhibitor necrostatin-1S (Nec-1S; Fig. 6L–O; Supplementary Fig. 8G, H). Notably, Nec-1S did not significantly reduce transaminase release, indicating a partial uncoupling between transaminase liberation and ACBP/DBI release in this model.

In conclusion, apoptosis, ferroptosis and necroptosis each induce the release of intracellular ACBP/DBI into the circulation, demonstrating that diverse forms of regulated cell death in vivo converge on a shared mechanism of ACBP/DBI liberation.

Correlation of plasma ACBP/DBI levels with organ damage across human cohorts

Driven by the observation that ELISA-quantifiable plasma ACBP/DBI levels rise with age [5, 7], body mass index (BMI) [8, 17] and multiple disease risk factors [16, 19, 21], we performed a systematic meta-analysis of ACBP/DBI concentrations across human cohorts. Protein measurements were obtained using two validated high-throughput platforms: (i) dual-antibody proximity extension assays (Olink) and (ii) DNA aptamer-based SomaScan, which yield highly comparable quantitative ACBP/DBI values and are corroborated by ELISA [9, 20, 23]. We analyzed correlations with disease biomarkers (continuous variable, Fig. 7A; Supplementary Table 1A), the presence of diagnosed disease at sampling (binary, Fig. 7B; Supplementary Table 1B) and the risk of future disease development (binary, Fig. 7C; Supplementary Table 1C).

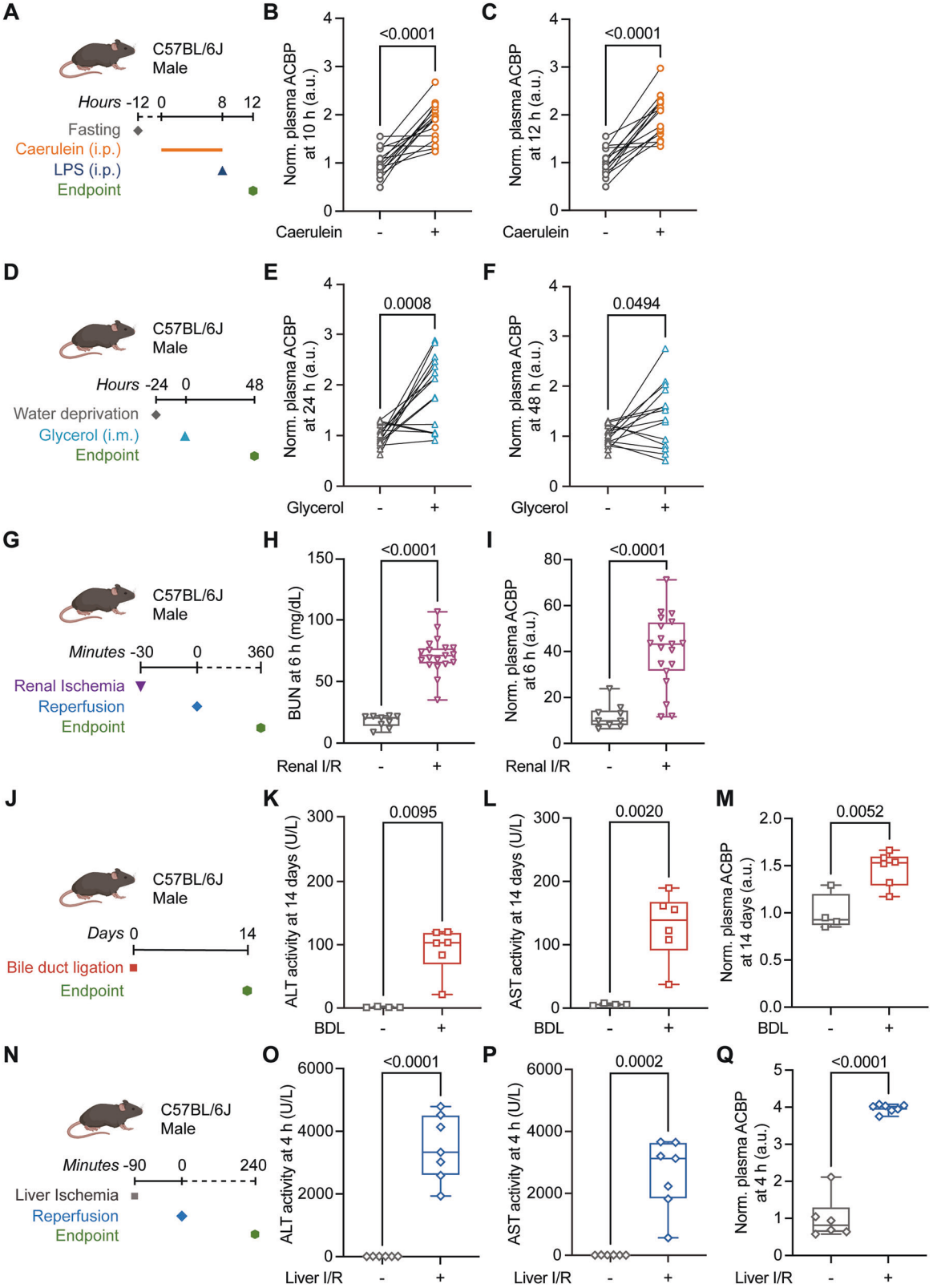

Across >100,000 individuals, ACBP/DBI positively correlated with chronological age, while in two cohorts (>50,000 participants each) ACBP/DBI negatively correlated with telomere length in peripheral blood mononuclear cells (Fig. 7A; Supplementary Table 1A). Moreover, ACBP/DBI correlated with obesity indices (BMI, waist circumference, body fat percentage, abdominal adiposity), laboratory markers of hyperglycemia and diabetes (glycemia, glycated hemoglobin HbA1c), systemic inflammation (CRP, total leukocytes, neutrophil to lymphocyte ratio), dyslipidemia (triglycerides, LDL, low HDL), cardiovascular risk (blood

Fig. 2 Plasma ACBP/DBI levels are elevated across multiple mouse models of organ injury. A–C Acute pancreatitis model. **A** Schematic representation of the experiment. Baseline blood samples were collected one week before treatment. 8-week-old male C57BL/6J mice were fasted for 12 h and received eight intraperitoneal injections of caerulein (100 µg/kg B.W.) at 1-h intervals, followed by a single injection of LPS (10 µg/mouse). Plasma ACBP/DBI was measured at 10 h (**B**) and 12 h (**C**) after caerulein administration and levels were normalized to baseline ($n = 15$ mice per group). **D–F** Rhabdomyolysis model. **D** Baseline blood samples were collected one week before treatment. 10-week-old male C57BL/6J mice were fasted with water for 24 h, then injected intramuscularly with 50% Glycerol (5 mL/kg B.W.) into both thighs. Plasma ACBP/DBI was assessed at 24 h (**E**) and 48 h (**F**) post-injection, normalized to baseline ($n = 14–15$ mice per group). **G–I** Renal ischemia-reperfusion model. **G** 12-week-old C57BL/6 male mice underwent sham surgery or bilateral renal ischemia for 30 min, followed by 6 h of reperfusion. BUN (**H**) was measured 6 h after reperfusion. ACBP/DBI (**I**) was measured at the same time point and normalized to the control group ($n = 9–19$ mice per group). **J–M** Bile duct ligation model. **J** 10-week-old male C57BL/6J mice underwent Sham or BDL surgery. Plasma ALT (**K**) and AST (**L**) were measured 14 days after surgery. Plasma ACBP/DBI was determined the same time point (**M**), normalized to control ($n = 4–6$ mice per group). **N–Q** Hepatic ischemia–reperfusion model. **N** 12-week-old male C57BL/6J mice underwent hepatic ischemia for 90 min, followed by 4 h of reperfusion. Plasma ALT (**O**) and AST (**P**) levels were measured and plasma ACBP/DBI levels were determined after 4 h of reperfusion (**Q**), normalized to control ($n = 6–7$ mice per group). Data in panels (**B**, **C**, **E**, **F**) are shown as paired data plots with lines connecting measurements before and after treatment and were analyzed using paired Student's *t* tests. Other panels are presented as box-and-whisker plots and comparisons between independent groups were performed using unpaired Student's *t* tests or Mann–Whitney U tests, as appropriate.BUN blood urea nitrogen, BDL bile duct ligation, I/R ischemia–reperfusion.

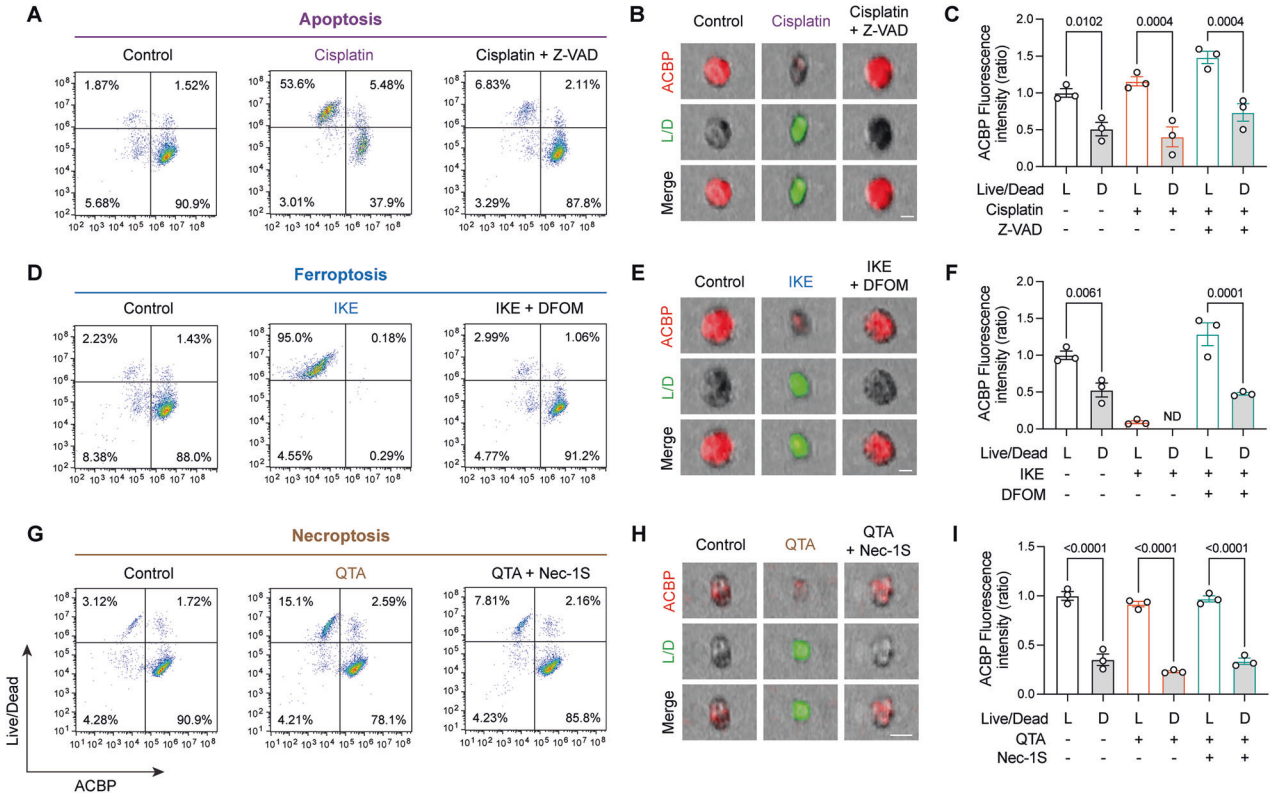

Fig. 3 Intracellular ACBP/DBI levels decrease in cells undergoing apoptosis, ferroptosis or necroptosis. A–C Apoptosis in Huh7 cells. Cells were pre-treated with Z-VAD (50 µM) for 1 h, then exposed to cisplatin (50 µM) for 48 h. Plasma membrane permeabilization was assessed using a green Live/Dead dye and intracellular ACBP/DBI was detected with a red-fluorescent antibody. Signals were quantified by fluorescence cytometry (**A**) and confirmed by image cytometry (**B**). Panel (**C**) shows the normalized fluorescence intensity of ACBP/DBI in live and dead cells, with values expressed relative to the control. **D–F** Ferroptosis in Huh7 cells. Cells were pre-incubated with DFOM (100 µM) for 1 h before treatment with IKE (10 µM) for 48 h. Plasma membrane integrity and intracellular ACBP/DBI were analyzed by fluorescence cytometry (**D**) and validated by image cytometry (**E**). Panel (**F**) shows the normalized fluorescence intensity of ACBP/DBI in live and dead cells, with values expressed relative to the control. **G–I** Necroptosis in Jurkat cells. Cells were pre-treated with Nec-1S (10 µM), Q-VD-OPh (10 µM) and AT406 (10 µM) for 1 h, followed by TNF-α (100 ng/mL) for 24 h. Plasma membrane permeabilization and intracellular ACBP/DBI were assessed by flow cytometry (**G**) and image cytometry (**H**). Panel (**I**) shows the normalized fluorescence intensity of ACBP/DBI in live and dead cells, with values expressed relative to the control. Data are presented as mean ± SEM. Comparisons among multiple groups were performed using one-way ANOVA, followed by Šidák's post hoc test for pairwise comparisons. ND non-detectable, QTA the combination of Q-VD-OPh, TNF-α and AT406.

pressure, arterial stiffness, heart rate, troponin T), renal dysfunction (creatinine, urea, cystatin C, reduced glomerular filtration rate) and liver dysfunction (ALT, AST, γ-GT, bilirubin, low albumin) (Fig. 7A; Supplementary Table 1A). Compared with healthy controls, patients with systemic conditions including autoimmune, infectious, inflammatory, malignant, metabolic or neuropsychiatric disorders, as well as frailty or multimorbidity, exhibited elevated plasma ACBP/DBI (Fig. 7B; Supplementary Table 1B). Organ-specific pathologies, affecting the brain (stroke), heart (ischemic heart disease), lungs (asthma, chronic obstructive pulmonary

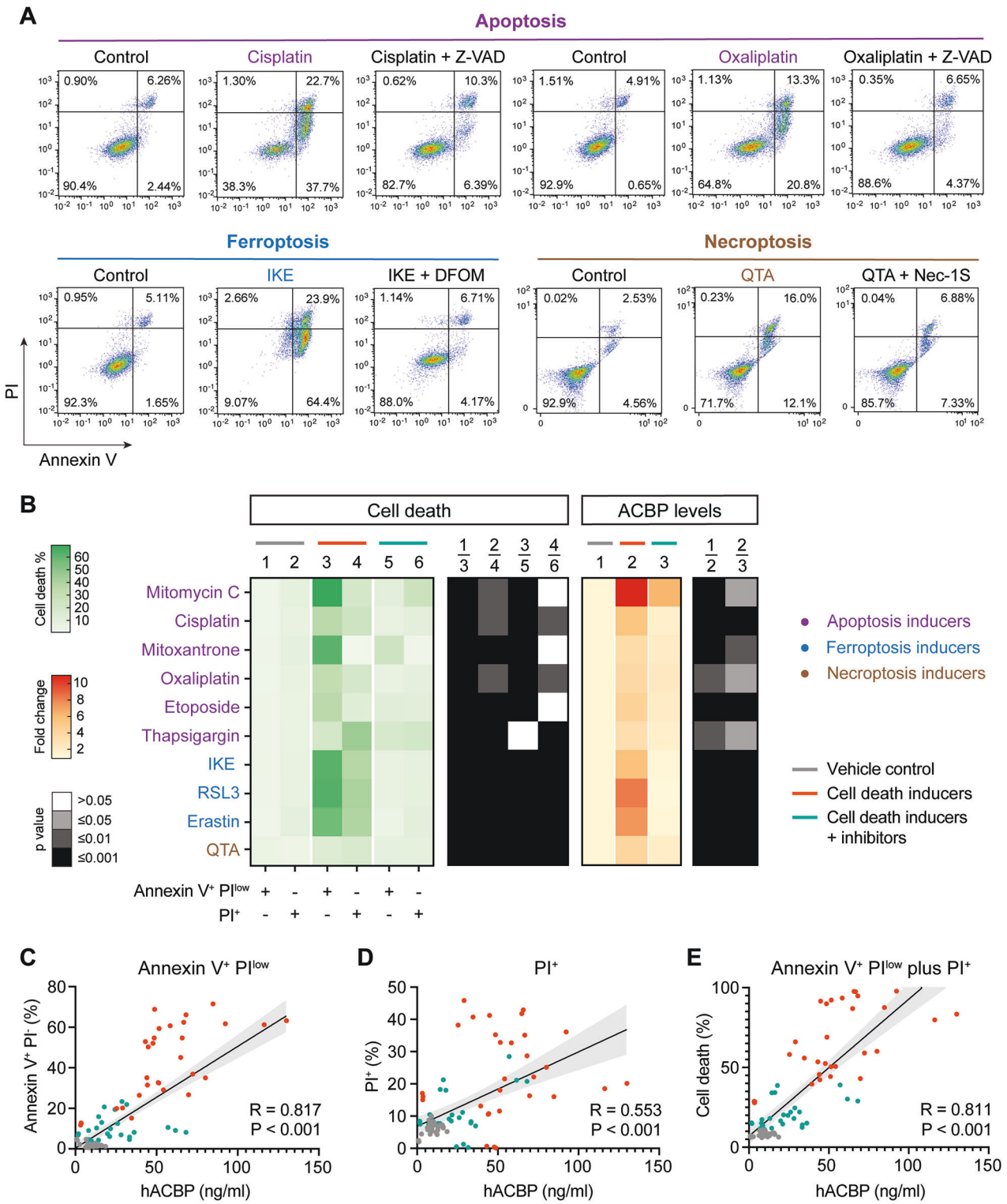

Fig. 4 Cell death induces ACBP/DBI release in both Huh7 and Jurkat cells. A Cells were treated as in Fig. 3. Apoptosis was assessed by Annexin V-FITC/PI staining using flow cytometry. **B** Huh7 cells were treated for 48 h with apoptosis inducers, including mitomycin C (50 μM), cisplatin (50 μM), mitoxantrone (2 μM), oxaliplatin (100 μM), etoposide (100 μM) and thapsigargin (10 μM) or with ferroptosis inducers, including IKE (10 μM), RSL3 (0.2 μM) and erastin (7.5 μM). Jurkat cells were subjected to necroptosis induction for 24 h with a combination of Q-VD-OPh (10 μM), TNF-α (100 ng/mL) and AT406 (10 μM), with or without their respective inhibitors. Early apoptotic (Annexin V$^+$ PI^{low}) and late apoptotic/necroptotic (PI$^+$) cells were quantified and ACBP levels in cell culture supernatants are shown as a heatmap. Correlation analyses demonstrate that extracellular ACBP/DBI positively associates with early cell death (**C**), late membrane rupture (**D**) and total cell death events (**E**). Group comparisons in Heatmaps were performed using one-way ANOVA followed by Šidák's post hoc test. Correlations were assessed using Spearman's rank correlation, with R values and p-values indicated in each panel. QTA the combination of Q-VD-OPh, AT406 and TNF-α.

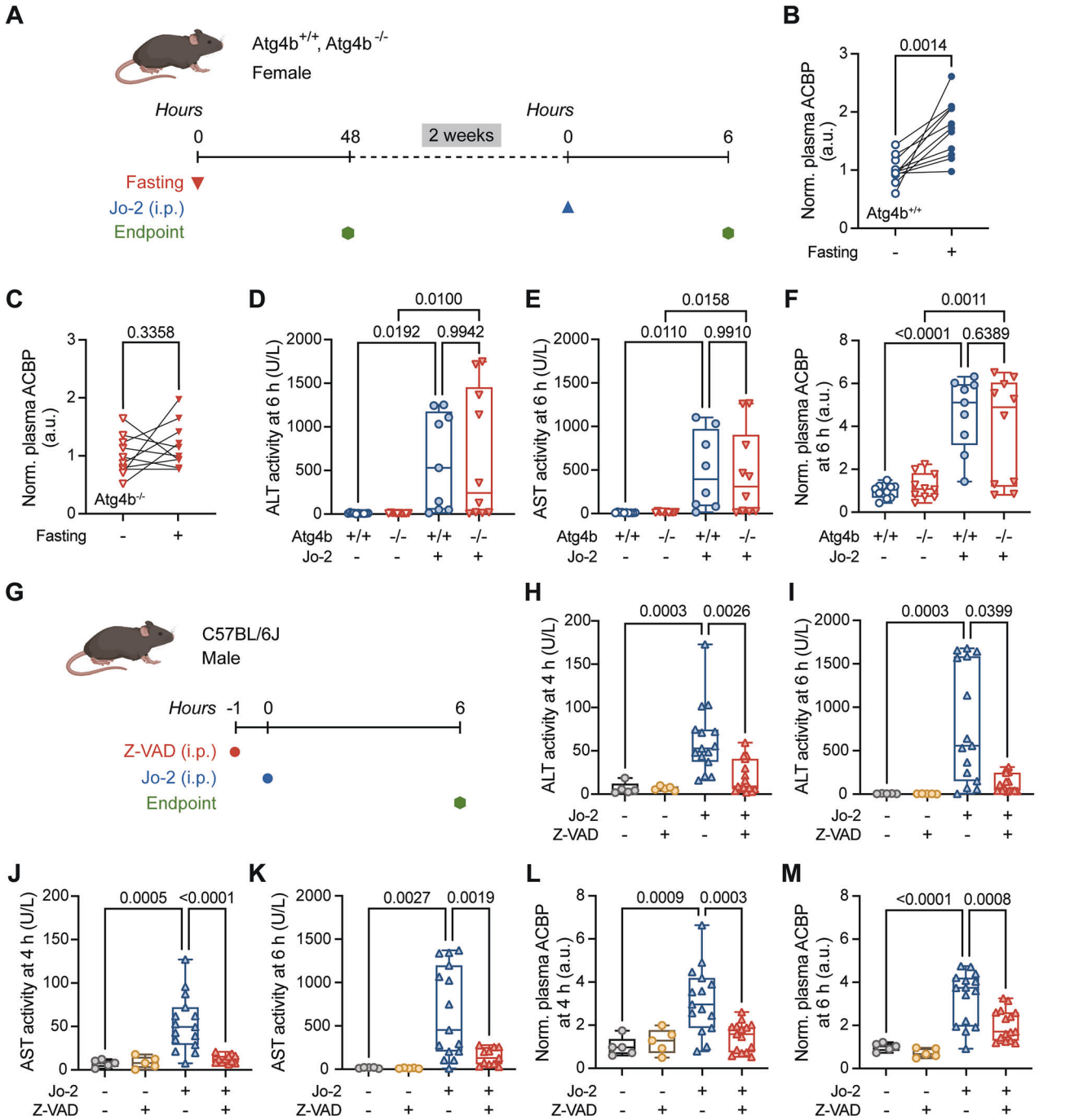

Fig. 5 Apoptosis increases plasma ACBP/DBI in mice. A Experimental schematic: *Atg4b*$^{+/+}$ and *Atg4b*$^{-/-}$ mice were starved for 48 h and blood was collected before and after starvation. Plasma ACBP levels in *Atg4b*$^{+/+}$ (**B**) and *Atg4b*$^{-/-}$ (**C**) mice are shown, normalized to baseline ($n = 10$–11 mice per group). After a two-week recovery period, *Atg4b*$^{+/+}$ and *Atg4b*$^{-/-}$ mice received intraperitoneal injection of Jo-2 (0.15 µg/g B.W.). Plasma ALT (**D**) and AST (**E**) were measured 6 h after injection and plasma ACBP/DBI was determined at the same time point (**F**), normalized to control ($n = 8$–11 mice per group). **G** 10-week-old male C57BL/6J mice received Z-VAD (5 mg/kg B.W.) intraperitoneally 1 h prior to Jo-2 (0.15 µg/g B.W.). Plasma ALT (**H**, **I**) and AST (**J**, **K**) were measured at 4 h and 6 h after Jo-2 injection. Plasma ACBP/DBI levels at 4 h (**L**) and 6 h (**M**) are shown, normalized to control ($n = 5$ to 15 mice per group). Panels **B** and **C** show paired data plots with lines connecting pre- and post-starvation measurements and were analyzed using paired Student's *t* tests. Other panels are shown as box-and-whisker plots and comparisons among groups were performed using one-way ANOVA with Šidák's post hoc test or Kruskal–Wallis followed by Dunn's post hoc test.

disease), kidney (acute tubular injury, chronic nephropathy, renal failure, transplantation) or liver (steatohepatitis, fibrosis, cirrhosis, hepatocellular carcinoma), were also associated with increased circulating ACBP/DBI (Fig. 7B; Supplementary Table 1B). Remarkably, even apparently healthy individuals with subclinical risk for joint replacement, cardiovascular events, cancer, frailty or mortality displayed elevated plasma ACBP/DBI (Fig. 7C; Supplementary Table 1C) [5, 7–9, 16, 17, 19, 21, 41, 53–78].

In summary, this meta-analysis establishes plasma ACBP/DBI as a sensitive, systemic biomarker of organ injury and cellular stress in humans, corroborating and extending mechanistic insights derived from mouse models.

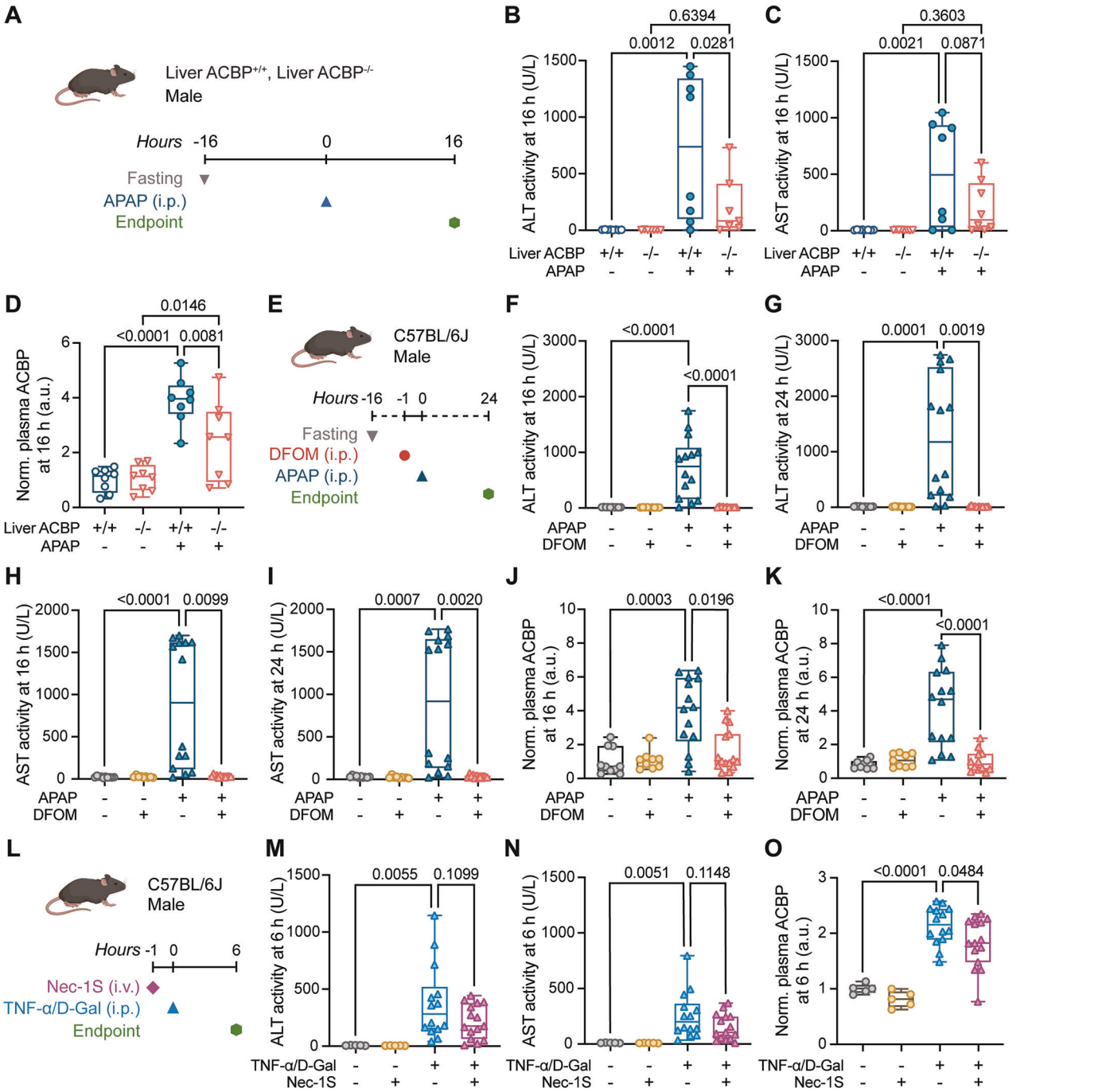

Fig. 6 Ferroptosis and necroptosis induce an increase in plasma ACBP/DBI in mice. A Schematic of the experiment: Liver ACBP$^{+/+}$ and ACBP$^{-/-}$ mice were fasted for 16 h and injected intraperitoneally with APAP (300 mg/kg B.W.). Plasma ALT (**B**) and AST (**C**) were measured 16 h post-injection and plasma ACBP/DBI was determined at the same time (**D**), normalized to control ($n = 7$–8 mice per group). **E** 12-week-old male C57BL/6J mice received DFOM (200 mg/kg B.W.) 1 h prior to APAP (300 mg/kg B.W.). Plasma ALT (**F**, **G**) and AST (**H**, **I**) were measured at 16 h and 24 h and plasma ACBP/DBI levels are shown at 16 h (**J**) and 24 h (**K**), normalized to control ($n = 9$–14 mice per group). **L** 10-week-old male C57BL/6J mice received a combination of TNF-α (30 μg/kg B.W.) and D-Gal (250 mg/kg B.W.), with Nec-1S (6 mg/kg B.W.) administered intravenously 1 h prior. Plasma ALT (**M**) and AST (**N**) and plasma ACBP/DBI (**O**) were measured 6 h after treatment, normalized to control ($n = 5$–15 mice per group). Data are presented as box-and-whisker plots and comparisons among multiple groups were performed using one-way ANOVA with Šidák's post hoc test or Kruskal–Wallis followed by Dunn's post hoc test.

DISCUSSION

ACBP/DBI is a leaderless polypeptide, meaning that it cannot undergo conventional, Golgi-dependent protein secretion. However, ACBP/DBI can be actively secreted by stressed cells in an autophagy-dependent fashion, meaning that pharmacological inhibition of autophagy or knockout of the autophagy-relevant gene *Atg4b* can prevent the surge of plasma ACBP/DBI concentrations in specific circumstances, for example, in response to fasting or glucocorticoid administration [8, 11, 12]. In this work, we identify an additional, passive mechanism of ACBP/DBI release from dying cells. Indeed, our study identifies ACBP/DBI as a systemic biomarker of cell death and organ injury in humans and

mice across multiple disease contexts and experimental models. We demonstrate that plasma ACBP/DBI levels rise in response to both apoptotic and non-apoptotic cell death, including ferroptosis and necroptosis and correlate with organ-specific protein signatures in humans. These findings provide a mechanistic link between regulated cell death and the circulating proteome, highlighting ACBP/DBI as a central effector released upon loss of plasma membrane integrity.

In SARS-CoV-2-infected individuals, plasma ACBP/DBI concentrations increased with disease severity and were elevated in patients with comorbidities such as diabetes, obesity, cardiovascular disease, chronic-obstructive pulmonary disease and cancer

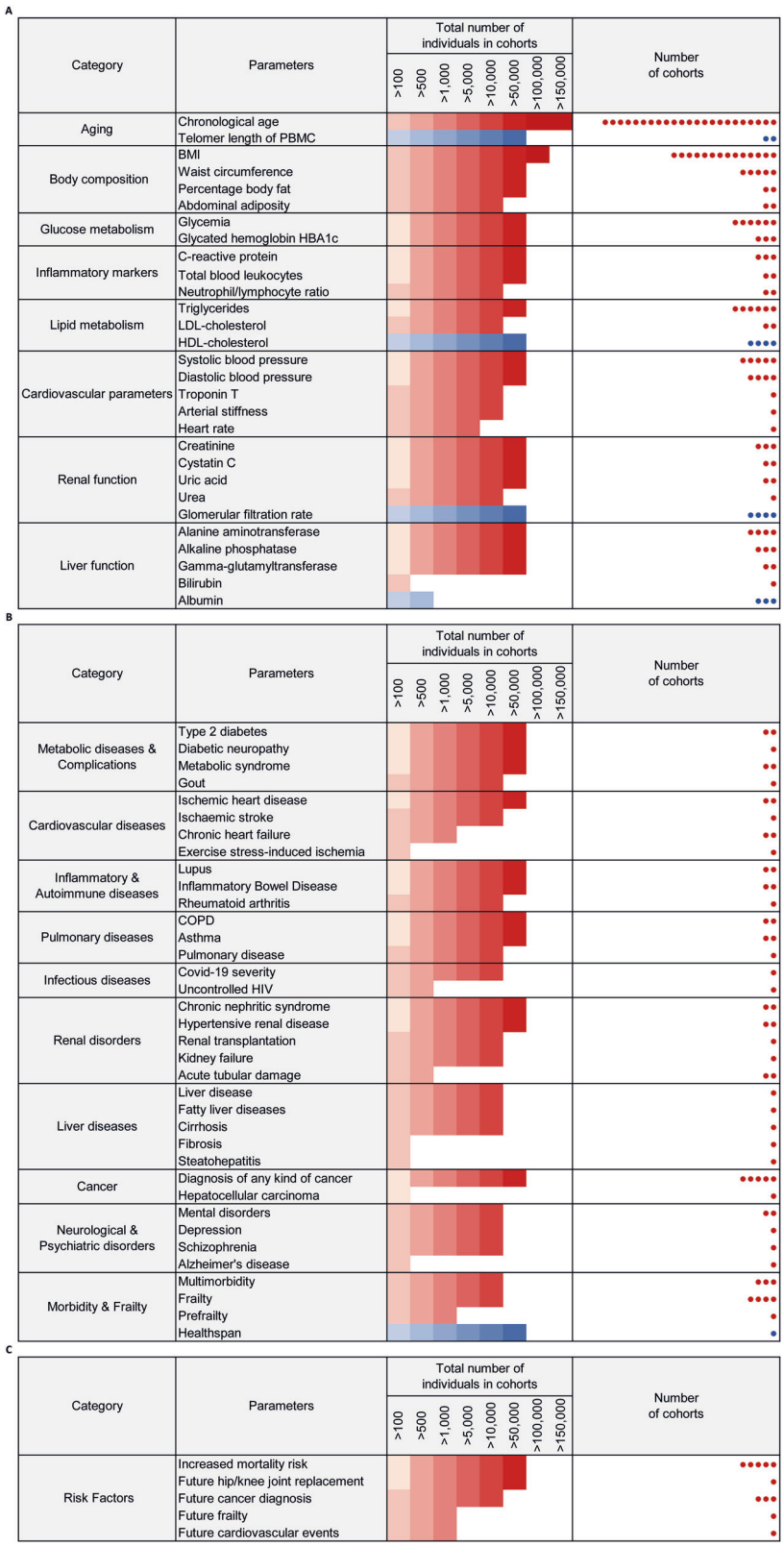

Fig. 7 Association of plasma ACBP/DBI levels with aging, disease states and future morbidity across human cohorts. A Correlations between plasma ACBP/DBI concentrations and clinical, biochemical and physiological parameters related to aging, body composition, glucose and lipid metabolism, inflammation, cardiovascular function, renal function and liver function. For each parameter, the heatmap indicates the direction and relative strength of the association with plasma ACBP/DBI across cohorts. **B** Associations between plasma ACBP/DBI levels and the presence of diagnosed diseases. Disease categories include metabolic diseases and complications, cardiovascular diseases, inflammatory and autoimmune diseases, pulmonary diseases, infectious diseases, renal disorders, liver diseases, cancer, neurological and psychiatric disorders and morbidity and frailty. **C** Associations between plasma ACBP/DBI levels and the risk of future adverse outcomes, including increased mortality risk, future hip or knee joint replacement, future cancer diagnosis, future frailty and future cardiovascular events. The total number of individuals analyzed, the number of cohorts and the corresponding references are indicated. Dot density reflects the number of cohorts reporting a significant association and color represents the relative magnitude and direction of the association (red, positive and blue, negative). Only associations supported by published cohort studies are included, as explained in Materials and Methods.

[23]. The positive correlations of ACBP/DBI with inflammatory markers (CRP, neutrophil to lymphocyte ratio, IL-6, SASP) and indices of organ dysfunction including renal, hepatic and cardiac parameters, suggest that ACBP/DBI release reflects both systemic inflammation and multi-organ stress. Notably, proteomic correlation analyses revealed that ACBP/DBI levels are enriched for proteins predominantly derived from skeletal muscle and pancreas, pointing to tissue-specific contributions to plasma ACBP/DBI, a concept supported by our quantitative organ analysis in mice. The association of ACBP/DBI with pancreatic and muscle markers may reflect the capacity of SARS-CoV-2 to infect and replicate in cells of the exocrine pancreas [79] and to cause pancreatitis [79], myositis [80] and rhabdomyolysis [81].

Mechanistically, our in vitro studies demonstrate that ACBP/DBI release is coupled to plasma membrane permeabilization rather than specific cell death pathways. Apoptotic, ferroptotic and necroptotic cells all exhibited loss of intracellular ACBP/DBI and concurrent accumulation in the extracellular medium. These in vitro observations were recapitulated in vivo: hepatocyte apoptosis induced by Jo-2 antibody, APAP-triggered ferroptosis and TNF-α + D-Gal–induced necroptosis each resulted in measurable increases in plasma ACBP/DBI in mice. Importantly, pharmacologic interventions that block cell death, such as Z-VAD for apoptosis or DFOM for ferroptosis, prevented both organ injury and ACBP/DBI release, providing causal evidence linking regulated cell death to circulating ACBP/DBI.

Our liver-specific ACBP/DBI knockout experiments revealed that hepatocytes are a major source of ACBP/DBI during APAP-induced injury. Nevertheless, the contribution of other organs such as kidney, pancreas and skeletal muscle is substantial, as demonstrated in various mouse models. These findings underscore the organ-specific yet multi-tissue nature of ACBP/DBI release, which may explain its broad correlation with diverse pathological states in humans.

Meta-analysis of human plasma proteomics confirms that ACBP/DBI is a robust indicator of systemic cellular stress. Across >100,000 individuals, elevated plasma ACBP/DBI correlates with aging, metabolic and cardiovascular risk factors, renal and hepatic dysfunction and increased risk for future morbidity and mortality. In individuals with organ-specific pathologies, including stroke, ischemic heart disease, COPD, renal injury and liver disease, plasma ACBP/DBI levels were consistently elevated, validating the translational relevance of our mouse and in vitro findings. Remarkably, even ostensibly healthy individuals at risk of cardiovascular or malignant disease displayed higher-than-normal ACBP/DBI plasma concentrations, suggesting its potential utility as an early-warning biomarker for impending organ stress or disease.

From a mechanistic perspective, ACBP/DBI may not merely serve as a passive biomarker but could instead actively participate in inter-organ communication during cellular stress. Prior studies indicate that extracellular ACBP/DBI modulates autophagy [26, 27] and energy metabolism [37, 49] and its rapid release upon membrane permeabilization could function as a distress signal to distant organs. This hypothesis aligns with our observation that ACBP/DBI correlates with proteins from muscle and pancreas organs known to secrete endocrine mediators under stress [82–84]. It is well established that pathologies affecting one organ tend to accelerate the manifestation of diseases in other organs [85–89], raising the possibility that ACBP/DBI contributes to this pathogenic inter-organ communication.

Several implications emerge from our findings. First, plasma ACBP/DBI provides a quantitative and mechanistic readout of cell death across multiple modalities and tissues. Second, it offers clinical translational potential as a biomarker for acute organ injury, systemic inflammatory states and risk stratification in both COVID-19 and broader pathologies. Third, the tissue-specific analysis of ACBP/DBI-correlated proteins may allow for organ-targeted biomarker profiling, potentially distinguishing liver versus muscle versus pancreatic injury in complex clinical scenarios.

In conclusion, our integrated analysis establishes ACBP/DBI as a central, conserved marker of cell death and organ injury, linking mechanistic cellular biology to clinically relevant human phenotypes. This work sets the stage for future studies exploring ACBP/DBI as both a biomarker and a potential mediator of stress response, with broad implications for translational medicine and the monitoring of organ health.

Limitations of the study

While our study integrates human cohorts, mouse models and in vitro assays to define ACBP/DBI as a systemic biomarker of cell death, several limitations remain. First, organ-specific contributions in humans are inferred from proteomic correlations and therefore require direct tissue-level validation. Second, although pharmacologic inhibitors link specific cell death pathways to ACBP/DBI release, off-target effects cannot be fully excluded. Third, longitudinal dynamics of ACBP/DBI during chronic disease remain unexplored and the causal roles of extracellular ACBP/DBI in inter-organ cross-talk are not directly tested. Finally, population heterogeneity may affect generalizability across ethnicities, ages and comorbidity profiles.

DATA AVAILABILITY

The data that support the findings of this study are available from the corresponding authors upon reasonable request.

REFERENCES

1. Tonon MC, Vaudry H, Chuquet J, Guillebaud F, Fan J, Masmoudi-Kouki O, et al. Endozepines and their receptors: structure, functions and pathophysiological significance. Pharmacol Ther. 2020;208:107386.
2. Duman C, Yaqubi K, Hoffmann A, Acikgoz AA, Korshunov A, Bendszus M, et al. Acyl-CoA-binding protein drives glioblastoma tumorigenesis by sustaining fatty acid oxidation. Cell Metab. 2019;30:274–89 e5.
3. Li S, Mingoia S, Montegut L, Lambertucci F, Chen H, Dong Y, et al. Atlas of expression of acyl CoA binding protein/diazepam binding inhibitor (ACBP/DBI) in human and mouse. Cell Death Dis. 2025;16:134.
4. Li S, Joseph A, Martins I, Kroemer G. Elevated plasma levels of the appetite-stimulator ACBP/DBI in fasting and obese subjects. Cell Stress. 2021;5:89–98.

5. Joseph A, Moriceau S, Sica V, Anagnostopoulos G, Pol J, Martins I, et al. Metabolic and psychiatric effects of acyl coenzyme A binding protein (ACBP)/diazepam binding inhibitor (DBI). Cell Death Dis. 2020;11:502.
6. Lebrun B, Barbot M, Tonon MC, Prevot V, Leprince J, Troadec JD. Glial endozepines and energy balance: Old peptides with new tricks. Glia. 2021;69:1079–93.
7. Montegut L, Lambertucci F, Moledo-Nodar L, Fiuza-Luces C, Rodriguez-Lopez C, Serra-Rexach JA, et al. Acyl-CoA-binding protein as a driver of pathological aging. Proc Natl Acad Sci USA. 2025;122:e2501584122.
8. Bravo-San Pedro JM, Sica V, Martins I, Pol J, Loos F, Maiuri MC, et al. Acyl-CoA-binding protein is a lipogenic factor that triggers food intake and obesity. Cell Metab. 2019;30:754–67 e9.
9. Isnard S, Royston L, Lin J, Fombuena B, Bu S, Kant S, et al. Distinct plasma concentrations of acyl-CoA-binding protein (ACBP) in HIV progressors and elite controllers. Viruses. 2022;14:453.
10. Montegut L, Abdellatif M, Motino O, Madeo F, Martins I, Quesada V, et al. Acyl coenzyme A binding protein (ACBP): an aging- and disease-relevant "autophagy checkpoint". Aging Cell. 2023;22:e13910.
11. Duran JM, Anjard C, Stefan C, Loomis WF, Malhotra V. Unconventional secretion of Acb1 is mediated by autophagosomes. J Cell Biol. 2010;188:527–36.
12. Zhang M, Schekman R. Cell biology. Unconventional secretion, unconventional solutions. Science. 2013;340:559–61.
13. Fabrizio P, Hoon S, Shamalnasab M, Galbani A, Wei M, Giaever G, et al. Genome-wide screen in Saccharomyces cerevisiae identifies vacuolar protein sorting, autophagy, biosynthetic, and tRNA methylation genes involved in life span regulation. PLoS Genet. 2010;6:e1001024.
14. Shamalnasab M, Dhaoui M, Thondamal M, Harvald EB, Faergeman NJ, Aguilaniu H, et al. HIF-1-dependent regulation of lifespan in Caenorhabditis elegans by the acyl-CoA-binding protein MAA-1. Aging. 2017;9:1745–69.
15. Booth LN, Shi C, Tantilert C, Yeo RW, Miklas JW, Hebestreit K, et al. Males induce premature demise of the opposite sex by multifaceted strategies. Nat Aging. 2022;2:809–23.
16. Montegut L, Joseph A, Chen H, Abdellatif M, Ruckenstuhl C, Motino O, et al. High plasma concentrations of acyl-coenzyme A binding protein (ACBP) predispose to cardiovascular disease: Evidence for a phylogenetically conserved proaging function of ACBP. Aging Cell. 2023;22:e13751.
17. Joseph A, Chen H, Anagnostopoulos G, Montegut L, Lafarge A, Motino O, et al. Effects of acyl-coenzyme A binding protein (ACBP)/diazepam-binding inhibitor (DBI) on body mass index. Cell Death Dis. 2021;12:599.
18. Schurfeld R, Sandner B, Hoffmann A, Kloting N, Baratashvili E, Nowicki M, et al. Renal function is a major predictor of circulating acyl-CoA-binding protein/diazepam-binding inhibitor. Front Endocrinol. 2023;14:1152444.
19. Montegut L, Liu P, Zhao L, Perez-Lanzon M, Chen H, Mao M, et al. Acyl-coenzyme a binding protein (ACBP) - a risk factor for cancer diagnosis and an inhibitor of immunosurveillance. Mol Cancer. 2024;23:187.
20. Fidelle M, Chen H, Montegut L, Boulate D, Abdayem P, Martineau M, et al. Increased plasma concentrations of acyl-coenzyme A binding protein (ACBP) predict future lung cancer development in smokers at risk of cardiovascular disease. Mol Cancer. 2025;24:296.
21. Motino O, Lambertucci F, Joseph A, Durand S, Anagnostopoulos G, Li S, et al. ACBP/DBI neutralization for the experimental treatment of fatty liver disease. Cell Death Differ. 2025;32:434–46.
22. Motino O, Lambertucci F, Anagnostopoulos G, Li S, Nah J, Castoldi F, et al. ACBP/DBI protein neutralization confers autophagy-dependent organ protection through inhibition of cell loss, inflammation, and fibrosis. Proc Natl Acad Sci USA. 2022;119:e2207344119.
23. Isnard S, Mabanga T, Royston L, Berini CA, Bu S, Aiyana O, et al. Extracellular acyl-CoA-binding protein as an independent biomarker of COVID-19 disease severity. Front Immunol. 2024;15:1505752.
24. Wu T, Huang T, Ren H, Shen C, Qian J, Fu X, et al. Metabolic coordination structures contribute to diabetic myocardial dysfunction. Circ Res. 2025;136:946–67.
25. Corral Nieto Y, Fernandez Pereira AG, Ventura-San Pedro L, Paredes SB, Perez-Cobas AE, Perez-Lanzon M, et al. Identification of ACBP as a potential target in ciliopathic obesity through multi-omics network analysis. Nat Commun. 2026:17;362.
26. Udupa P, Kumar A, Parit R, Ghosh DK. Acyl-CoA binding protein regulates nutrient-dependent autophagy. Metabolism. 2023;145:155338.
27. Zhang Y, Ruan LL, Li MR, Yao L, Li FF, Xie YL, et al. Palmitic acid impairs human and mouse placental function by inhibiting trophoblast autophagy through induction of acyl-coenzyme A-binding protein (ACBP) upregulation. Hum Reprod. 2024;39:1423–31.
28. Su C-Y, Zhou S, Gonzalez-Kozlova E, Butler-Laporte G, Brunet-Ratnasingham E, Nakanishi T, et al. Circulating proteins to predict adverse COVID-19 outcomes. medRxiv. 2021. https://www.medrxiv.org/content/10.1101/2021.10.04.21264015v1.
29. Zhang B, He P, Lawrence JEG, Wang S, Tuck E, Williams BA, et al. A human embryonic limb cell atlas resolved in space and time. Nature. 2024;635:668–78.
30. Team RC R. A language and environment for statistical computing. 2023. https://www.R-project.org/
31. Wei T. R package 'corrplot': Visualization of a Correlation Matrix. 2024. https://github.com/taiyun/corrplot.
32. Swetha K, Indumathi MC, Kishan R, Siddappa S, Chen CH, Marathe GK. Selenium mitigates caerulein and LPS-induced severe acute pancreatitis by inhibiting MAPK, NF-kappaB, and STAT3 signaling via the Nrf2/HO-1 pathway. Biol Trace Elem Res. 2025;203:4728–50.
33. Song SJ, Kim SM, Lee SH, Moon JY, Hwang HS, Kim JS, et al. Rhabdomyolysis-induced AKI was ameliorated in NLRP3 KO mice via alleviation of mitochondrial lipid peroxidation in renal tubular cells. Int J Mol Sci. 2020;21:8564.
34. Wei Q, Dong Z. Mouse model of ischemic acute kidney injury: technical notes and tricks. Am J Physiol Renal Physiol. 2012;303:F1487–94.
35. Tag CG, Sauer-Lehnen S, Weiskirchen S, Borkham-Kamphorst E, Tolba RH, Tacke F, et al. Bile duct ligation in mice: induction of inflammatory liver injury and fibrosis by obstructive cholestasis. J Vis Exp. 2015:52438. https://doi.org/10.3791/52438.
36. Marino G, Fernandez AF, Cabrera S, Lundberg YW, Cabanillas R, Rodriguez F, et al. Autophagy is essential for mouse sense of balance. J Clin Invest. 2010;120:2331–44.
37. Chen H, Moriceau S, Joseph A, Mailliet F, Li S, Tolle V, et al. Acyl-CoA binding protein for the experimental treatment of anorexia. Sci Transl Med. 2024;16:eadl0715.
38. St Sauver JL, Weston SA, Atkinson EJ, Mc Gree ME, Mielke MM, et al. Biomarkers of cellular senescence and risk of death in humans. Aging Cell. 2023;22:e14006.
39. Tremblay K, Rousseau S, Zawati MH, Auld D, Chasse M, Coderre D, et al. The Biobanque quebecoise de la COVID-19 (BQC19)-A cohort to prospectively study the clinical and biological determinants of COVID-19 clinical trajectories. PLoS One. 2021;16:e0245031.
40. Tanguay P, Decary S, Lemaire-Paquette S, Leonard G, Piche A, Dubois MF, et al. Trajectories of health-related quality of life and their predictors in adult COVID-19 survivors: a longitudinal analysis of the Biobanque Quebecoise de la COVID-19 (BQC-19). Qual Life Res. 2023;32:2707–17.
41. Oh HS, Rutledge J, Nachun D, Palovics R, Abiose O, Moran-Losada P, et al. Organ aging signatures in the plasma proteome track health and disease. Nature. 2023;624:164–72.
42. Durbin PW, Jeung N, Kullgren B, Clemons GK. Gross composition and plasma and extracellular water volumes of tissues of a reference mouse. Health Phys. 1992;63:427–42.
43. Morla L, Shore O, Lynch IJ, Merritt ME, Wingo CS. A noninvasive method to study the evolution of extracellular fluid volume in mice using time-domain nuclear magnetic resonance. Am J Physiol Renal Physiol. 2020;319:F115–F24.
44. Martinez-Garcia GG, Perez RF, Fernandez AF, Durand S, Kroemer G, Marino G. Autophagy deficiency by Atg4B loss leads to metabolomic alterations in mice. Metabolites. 2021;11:481.
45. Ogasawara J, Watanabe-Fukunaga R, Adachi M, Matsuzawa A, Kasugai T, Kitamura Y, et al. Lethal effect of the anti-Fas antibody in mice. Nature. 1993;364:806–9.
46. Wanner GA, Mica L, Wanner-Schmid E, Kolb SA, Hentze H, Trentz O, et al. Inhibition of caspase activity prevents CD95-mediated hepatic microvascular perfusion failure and restores Kupffer cell clearance capacity. FASEB J. 1999;13:1239–48.
47. Lee WM. Acetaminophen and the U.S. Acute Liver Failure Study Group: lowering the risks of hepatic failure. Hepatology. 2004;40:6–9.
48. Yamada N, Karasawa T, Kimura H, Watanabe S, Komada T, Kamata R, et al. Ferroptosis driven by radical oxidation of n-6 polyunsaturated fatty acids mediates acetaminophen-induced acute liver failure. Cell Death Dis. 2020;11:144.
49. Pan H, Tian AL, Chen H, Xia Y, Sauvat A, Moriceau S, et al. Pathogenic role of acyl coenzyme A binding protein (ACBP) in Cushing's syndrome. Nat Metab. 2024;6:2281–99.
50. Dixon SJ, Lemberg KM, Lamprecht MR, Skouta R, Zaitsev EM, Gleason CE, et al. Ferroptosis: an iron-dependent form of nonapoptotic cell death. Cell. 2012;149:1060–72.
51. Wang H, An P, Xie E, Wu Q, Fang X, Gao H, et al. Characterization of ferroptosis in murine models of hemochromatosis. Hepatology. 2017;66:449–65.
52. Leist M, Gantner F, Bohlinger I, Tiegs G, Germann PG, Wendel A. Tumor necrosis factor-induced hepatocyte apoptosis precedes liver failure in experimental murine shock models. Am J Pathol. 1995;146:1220–34.
53. Sathyan S, Ayers E, Gao T, Milman S, Barzilai N, Verghese J. Plasma proteomic profile of frailty. Aging Cell. 2020;19:e13193.
54. Sathyan S, Ayers E, Gao T, Weiss EF, Milman S, Verghese J, et al. Plasma proteomic profile of age, health span, and all-cause mortality in older adults. Aging Cell. 2020;19:e13250.

55. Coenen L, Lehallier B, de Vries HE, Middeldorp J. Markers of aging: Unsupervised integrated analyses of the human plasma proteome. Front Aging. 2023;4:1112109.
56. Eldjarn GH, Ferkingstad E, Lund SH, Helgason H, Magnusson OT, Gunnarsdottir K, et al. Large-scale plasma proteomics comparisons through genetics and disease associations. Nature. 2023;622:348–58.
57. Liu F, Schrack JA, Walston J, Mathias RA, Windham BG, Grams ME, et al. Mid-life plasma proteins associated with late-life prefrailty and frailty: a proteomic analysis. Geroscience. 2024;46:5247–65.
58. Wang B, Pozarickij A, Mazidi M, Wright N, Yao P, Said S, et al. Comparative studies of 2168 plasma proteins measured by two affinity-based platforms in 4000 Chinese adults. Nat Commun. 2025;16:1869.
59. Ferkingstad E, Sulem P, Atlason BA, Sveinbjornsson G, Magnusson MI, Styrmisdottir EL, et al. Large-scale integration of the plasma proteome with genetics and disease. Nat Genet. 2021;53:1712–21.
60. Alvez MB, Bergstrom S, Kenrick J, Johansson E, Aberg M, Akyildiz M, et al. A human pan-disease blood atlas of the circulating proteome. Science. 2025;390:eadx2678.
61. Sathyan S, Milman S, Ayers E, Gao T, Verghese J, Barzilai N. Plasma proteomic profile of abdominal obesity in older adults. Obesity. 2024;32:938–48.
62. Lim CGY, Ozkan B, Liang Y, Chen J, Yao J, Khaing NEE, et al. Plasma proteomic signatures of adiposity are associated with cardiovascular risk factors and type 2 diabetes risk in a multiethnic Asian population. Diabetes. 2025;74:416–26.
63. Kovac L, Gancheva S, Jahnert M, Sehgal R, Mastrototaro L, Schlensak M, et al. Different effects of bariatric surgery on epigenetic plasticity in skeletal muscle of individuals with and without type 2 diabetes. Diabetes Metab. 2024;50:101561.
64. Buckley LF, Dorbala P, Lamberson V, Claggett BL, Ren Y, Grams ME, et al. Linking chronic kidney disease to incident heart failure and adverse cardiac remodeling through the plasma proteome. The ARIC Study. JACC Heart Fail. 2025;13:102512.
65. Puerta R, Cano A, Garcia-Gonzalez P, Garcia-Gutierrez F, Capdevila M, de Rojas I, et al. Head-to-head comparison of aptamer- and antibody-based proteomic platforms in human cerebrospinal fluid samples from a real-world memory clinic cohort. Int J Mol Sci. 2024;26:286.
66. Gadd DA, Hillary RF, Kuncheva Z, Mangelis T, Cheng Y, Dissanayake M, et al. Blood protein assessment of leading incident diseases and mortality in the UK Biobank. Nat Aging. 2024;4:939–48.
67. Kang B, Yin X, Chen D, Wang Y, Lv J, Zhou J, et al. Balanced diets are associated with a lower risk of type 2 diabetes than plant-based diets. Diabetes Res Clin Pract. 2025;219:111977.
68. Lan H, Xu S, Li H, Guo R, Ma D, Feng Z, et al. Plasma proteomics identifies potential drug targets for diabetic polyneuropathy: evidence from prospective cohorts and genetic analysis. Diabetes Obes Metab. 2026;28:615–24.
69. Packer M, Ferreira JP, Butler J, Filippatos G, Januzzi JL Jr., Gonzalez Maldonado S, et al. Reaffirmation of mechanistic proteomic signatures accompanying SGLT2 inhibition in patients with heart failure: a validation cohort of the EMPEROR program. J Am Coll Cardiol. 2024;84:1979–94.
70. Addona TA, Shi X, Keshishian H, Mani DR, Burgess M, Gillette MA, et al. A pipeline that integrates the discovery and verification of plasma protein biomarkers reveals candidate markers for cardiovascular disease. Nat Biotechnol. 2011;29:635–43.
71. Schmidt IM, Surapaneni AL, Zhao R, Upadhyay D, Yeo WJ, Schlosser P, et al. Plasma proteomics of acute tubular injury. Nat Commun. 2024;15:7368.
72. Sveinbjornsson G, Ulfarsson MO, Thorolfsdottir RB, Jonsson BA, Einarsson E, Gunnlaugsson G, et al. Multiomics study of nonalcoholic fatty liver disease. Nat Genet. 2022;54:1652–63.
73. Kolijn PM, Smith-Byrne K, Burk V, Viallon V, Lee MA, Papier K, et al. Multi-cohort high-dimensional proteomics reveals early risk markers for lymphoid cancer subtypes. Nat Commun. 2025;16:9517.
74. Li S, Motino O, Lambertucci F, Pol J, Chen H, Pan L, et al. Neutralization of acyl coenzyme A binding protein for the experimental prevention and treatment of hepatocellular carcinoma. Cell Rep Med. 2025;6:102232.
75. Dammer EB, Shantaraman A, Ping L, Duong DM, Gerasimov ES, Ravindran SP, et al. Proteomic analysis of Alzheimer's disease cerebrospinal fluid reveals alterations associated with APOE epsilon4 and atomoxetine treatment. Sci Transl Med. 2024;16:eadn3504.
76. Kuo CL, Liu P, Drouard G, Vuoksimaa E, Kaprio J, Ollikainen M, et al. A proteomic signature of healthspan. Proc Natl Acad Sci USA. 2025;122:e2414086122.
77. Liu X, Axelsson GT, Newman AB, Psaty BM, Boudreau RM, Wu C, et al. Plasma proteomic signature of human longevity. Aging Cell. 2024;23:e14136.
78. Styrkarsdottir U, Lund SH, Thorleifsson G, Saevarsdottir S, Gudbjartsson DF, Thorsteinsdottir U, et al. Cartilage acidic protein 1 in plasma associates with prevalent osteoarthritis and predicts future risk as well as progression to joint replacements: results from the UK Biobank resource. Arthritis Rheumatol. 2023;75:544–52.
79. Muller JA, Gross R, Conzelmann C, Kruger J, Merle U, Steinhart J, et al. SARS-CoV-2 infects and replicates in cells of the human endocrine and exocrine pancreas. Nat Metab. 2021;3:149–65.
80. Syrmou V, Liaskos C, Ntavari N, Mitsimponas K, Simopoulou T, Alexiou I, et al. COVID-19 vaccine-associated myositis: a comprehensive review of the literature driven by a case report. Immunol Res. 2023;71:537–46.
81. Karimi M, Faal Hamedanchi N, Ansari K, Nahavandi R, Mazdak M, Javaherchian F, et al. Rhabdomyolysis secondary to COVID-19 infection and vaccination: a review of literature. Front Med. 2024;11:1460676.
82. Coate KC, Hernandez G, Thorne CA, Sun S, Le TDV, Vale K, et al. FGF21 is an exocrine pancreas secretagogue. Cell Metab. 2017;25:472–80.
83. Severinsen MCK, Pedersen BK. Muscle-organ crosstalk: the emerging roles of myokines. Endocr Rev. 2020;41:594–609.
84. Rai M, Demontis F. Therapeutic potential of myokines and myometabolites for brain ageing and neurodegeneration. Nat Rev Endocrinol. 2026;22:1–2.
85. Hadjiphilippou S, Kon SP. Cardiorenal syndrome: review of our current understanding. J R Soc Med. 2016;109:12–7.
86. Yeung EY, Mohammed RS. What tasks can physicians delegate to pharmacists?. Br J Gen Pract. 2018;68:519.
87. Targher G, Byrne CD, Tilg H. NAFLD and increased risk of cardiovascular disease: clinical associations, pathophysiological mechanisms and pharmacological implications. Gut. 2020;69:1691–705.
88. Lopez-Otin C, Kroemer G. Hallmarks of health. Cell. 2021;184:33–63.
89. Raevens S, Boret M, Fallon MB. Hepatopulmonary syndrome. JHEP Rep. 2022;4:100527.

ACKNOWLEDGEMENTS

This work was made possible thanks to the sharing of data and samples from the Quebec COVID-19 Biobank, funded by the Fonds de recherche du Québec-Santé, Génome Québec, the Public Health Agency of Canada and the Ministère de la Santé et des Services sociaux. We thank all BQC19 participants for their valuable contribution. The authors thank the CRC core facilities.

AUTHOR CONTRIBUTIONS

Investigation: YR, FL, YY, HC, YD, SM, SL, OM, LM, AJ, LF, and EGSD. Methodology: MD-M, MC, and MCM. Analysis of the COVID-19 cohort: VC, SI, AJ, AF, MA, and JPR. Meta-analysis: IM. Statistical analysis of experimental data: YR and FL. Visualization: YR and IM. Conceptualization: GK. Project administration: IM and GK. Supervision: IM and GK. Writing – original draft: YR, IM, and GK. Writing – review & editing: All authors.

FUNDING

GK is supported by the Ligue contre le Cancer (équipe labellisée); Agence National de la Recherche (ANR-22-CE14-0066 VIVORUSH, ANR-23-CE44-0030 COPPERMAC, ANR-23-R4HC-0006 Ener-LIGHT); Association pour la recherche sur le cancer (ARC); Cancéropôle Ile-de-France; Fondation pour la Recherche Médicale (FRM); European Research Council Advanced Investigator Award (ERC-2021-ADG, Grant No. 101052444; project acronym: ICD-Cancer, project title: Immunogenic cell death (ICD) in the cancer-immune dialogue); The ERA4 Health Cardinoff Grant Ener-LIGHT; European Union Horizon 2020 research and innovation programs Oncobiome (grant agreement number: 825410, Project Acronym: ONCOBIOME, Project title: Gut OncoMicrobiome Signatures [GOMS] associated with cancer incidence, prognosis and prediction of treatment response, Prevalung (grant agreement number 101095604, Project Acronym: PREVALUNG EU, project title: Biomarkers affecting the transition from cardiovascular disease to lung cancer: towards stratified interception), Neutrocure (grant agreement number 861878: Project Acronym: Neutrocure; project title: Development of "smart" amplifiers of reactive oxygen species specific to aberrant polymorphonuclear neutrophils for treatment of inflammatory and autoimmune diseases, cancer and myeloablation); National support managed by the Agence Nationale de la Recherche under the France 2030 programme (reference number 21-ESRE-0028, ESR/Equipex+ Onco-Pheno-Screen); Hevolution Network on Senescence in Aging (reference HF-E Einstein Network); Institut National du Cancer (INCa); Institut Universitaire de France; PAIR-Obésité INCa_18713, the RHUs Immunolife and LUCA-pi (ANR-21-RHUS-0017 and ANR-23-RHUS-0010, both dedicated to France Relance 2030); Seerave Foundation; SIRIC Cancer Research and Personalized Medicine (CARPEM, SIRIC CARPEM INCa-DGOS-Inserm-ITMO Cancer_18006 supported by Institut National du Cancer, Ministère des Solidarités et de la Santé and INSERM). This study contributes to the IdEx Université de Paris Cité ANR-18-IDEX-0001. LM is a National Mah Jongg League Fellow of the Damon Runyon Cancer Research Foundation (DRG-2560-25). EGSD was supported by the University of Las Palmas de Gran Canaria (ULPGC), financed by the

Ministry of Universities, granted by Order UNI/501/2021 of May 26, and by the European Union–Next Generation EU Funds. OM is supported by the "Beatriz Galindo Junior" Program from the Spanish Ministry of Universities (BG22/00104).

COMPETING INTERESTS

LM, IM and GK are the inventors of patents covering the immunotherapeutic utility of ACBP/DBI neutralization. GK has been holding research contracts with Daiichi Sankyo, Eleor, Kaleido, Lytix Pharma, PharmaMar, Osasuna Therapeutics, Samsara Therapeutics, Sanofi, Sutro, Tollys and Vascage. GK is on the Board of Directors of the Bristol Myers Squibb Foundation France. GK is a scientific co-founder of everImmune, Osasuna Therapeutics, Samsara Therapeutics and Therafast Bio. GK is in the scientific advisory boards of Hevolution, Institut Servier and Rejuveron Life Sciences/Centenara Labs AG. GK is the inventor of patents covering therapeutic targeting of aging, cancer, cystic fibrosis and metabolic disorders. Among these patents, one "Methods for weight reduction" (US11905330B1) is relevant to this study. GK's brother, Romano Kroemer, was an employee of Sanofi and now consults for Boehringer-Ingelheim. GK's wife, Laurence Zitvogel, has held research contracts with Glaxo Smyth Kline, Incyte, Lytix, Kaleido, Innovate Pharma, Daiichi Sankyo, Pilege, Merus, Transgene, 9 m, Tusk and Roche, was on the Board of Directors of Transgene, is a cofounder of everImmune and holds patents covering the treatment of cancer and the therapeutic manipulation of the microbiota. The funders had no role in the design of the study, in the writing of the manuscript or in the decision to publish the results.

ADDITIONAL INFORMATION

Supplementary information The online version contains supplementary material available at https://doi.org/10.1038/s41418-026-01775-w.

Correspondence and requests for materials should be addressed to Isabelle Martins or Guido Kroemer.